

Reactive nitrogen in and around the northeastern and Mid-Atlantic US: sources, sinks, and connections with ozone

Min Huang^{1,2}, Gregory R. Carmichael³, Kevin W. Bowman⁴, Isabelle De Smedt⁵, Andreas Colliander⁴, Michael H. Cosh⁶, Sujay V. Kumar¹, Alex B. Guenther⁷, Scott J. Janz¹, Ryan M. Stauffer¹, Anne M. Thompson¹, Niko M. Fedkin¹, Robert J. Swap¹, John D. Bolten¹, Alicia T. Joseph¹

¹Earth Sciences Division, NASA Goddard Space Flight Center, Greenbelt, MD 20771, USA

²Earth System Science Interdisciplinary Center, University of Maryland, College Park, MD 20740, USA

³College of Engineering, University of Iowa, Iowa City, IA 52242, USA

⁴Jet Propulsion Laboratory, California Institute of Technology, Pasadena, CA 91109, USA

10 ⁵Royal Belgian Institute for Space Aeronomy, 1180 Brussels, Belgium

⁶Hydrology and Remote Sensing Laboratory, US Department of Agriculture, Beltsville, MD 20705, USA

⁷Department of Earth System Science, University of California at Irvine, Irvine, CA 92697, USA

Correspondence to: Min Huang (minhuang@umd.edu)

Abstract. This study describes an application of a regional Earth system model (NASA-Unified Weather Research and Forecasting with online chemistry) with updated parameterizations for selected land-atmosphere exchange processes and multi-platform, multidisciplinary observations. First, we estimate reactive nitrogen (Nr = oxidized NO_y + reduced NH_x) emissions from anthropogenic and natural sources, nitrogen dioxide (NO₂) column densities and surface concentrations, total and speciated Nr dry or/and wet deposition fluxes during 2018–2023 over the northeastern and Mid-Atlantic US, most of which belong to nitrogen oxides-limited or transitional chemical regimes. The estimated multi-year Nr concentrations and deposition fluxes are then related to ozone (O₃), in terms of their spatiotemporal variability and key drivers as well as possible ecosystem impacts. Finally, through three sets of case studies, we identify and discuss about 1) the capability of land data assimilation (DA) to reduce the uncertainty in modeled land surface states at daily-to-interannual timescales that can propagate into atmospheric chemistry fields; 2) the impacts of irrigation on land surface and atmospheric fields as well as pollutants' ecosystem uptake and impacts; and 3) the impacts of transboundary air pollution during selected extreme events on pollutants' budgets and ecosystem impacts. With the updated model parameterizations and anthropogenic emission inputs, the eastern US surface O₃ modeled by this tool persistently agrees better with observations (i.e., with root-mean-square errors staying within 4–7 ppbv for the individual years' May-June-July) than many of those in literature where model errors are often tens of ppbv. The model-based correlation between daytime surface O₃ and early afternoon NO₂ columns, which shows a dependency on column HCHO/NO₂ ratios, is higher in 2020 than during 2018–2023 ($r=0.62$ and 0.54 , respectively). The O₃ vegetative uptake overall dropped by ~10% from 2018 to 2023, displaying clearer downward temporal changes than the total Nr deposition due to the declining NO_y emission and deposition fluxes competing with the increasing NH_x fluxes. It is highlighted that, temporal variability of Nr and O₃ concentrations and fluxes on subregional-to-local scales respond to hydrological variability that can be influenced by precipitation and controllable human activities such as

irrigation. Deposition processes and biogenic emissions that are highly sensitive to interconnected environmental and plants' physiological conditions, as well as extra-regional sources (e.g., O₃-rich stratospheric air and dense wildfire plumes from upwind regions), have been playing increasingly important roles in controlling pollutants' budgets in this area as local emissions go down owing to effective emission regulations and COVID lockdowns. To better inform the design of mitigation and adaptation strategies, it is recommended to continue evaluating and improving the model parameterizations and inputs relevant to these processes in seamlessly coupled multiscale Earth system models using laboratory and field experiments in combination with satellite DA which would in turn benefit remote sensing communities.

1 Background, motivation, and goals

Nitrogen oxides (NO_x) are an important group of ozone (O₃) precursor and destroyer, and ground-level O₃ is a US Environmental Protection Agency (EPA)-regulated criteria air pollutant. NO_x consists of nitric oxide (NO) and nitrogen dioxide (NO₂), the latter of which is another US EPA-regulated criteria air pollutant that has the highest exposure disparities (Liu et al., 2021). Emitted from various anthropogenic (anth) and natural sources, NO_x is readily transformable to/from other forms of reactive nitrogen (Nr = oxidized NO_y + reduced NH_x) species, such as ammonia (NH₃), peroxyacetyl nitrate (PAN) and nitric acid (HNO₃). Some of these chemical reactions also contribute to fine particulate matter pollution, which is connected with O₃ via aerosol radiative effects and heterogeneous chemistry (Seinfeld and Pandis, 2016; Monks et al., 2021). Many previous studies have demonstrated that NO_x emissions and concentrations play more crucial roles than volatile organic compounds (VOCs) in regulating the magnitude and spatiotemporal variability of O₃ (e.g., Duncan et al., 2010; Jin et al., 2017; Koplitz et al., 2022; Souri et al., 2023) as well as aerosols (Carlton et al., 2010; Holt et al., 2015) in much of the northeastern and Mid-Atlantic states, the most populous US region where the land surface is highly heterogeneous and hydroclimatic extremes and exceedances of the US National Ambient Air Quality Standards occur from time to time (US Global Change Research Program, 2023; US EPA, 2023). An improved understanding of the sources, sinks, and distributions of NO_x and Nr as well as how these have been and will be changing through time is beneficial for interpreting O₃ air pollution levels and their spatiotemporal variability in this area. The removals of Nr, O₃, and other chemicals involved in their life cycles from the atmosphere through wet or/and dry deposition closely interact with multiple other interconnected environmental stressors (e.g., temperature, humidity, precipitation, soil moisture, SM, and carbon dioxide, CO₂) and plants' physiological conditions. Together, they can cause intertwined and cascading effects on the diverse terrestrial and aquatic ecosystems (e.g., United Nations Economic Commission for Europe, 1999; Galloway et al., 2003, 2004; Felzer et al., 2009; Simpson et al., 2014; Lombardozzi et al., 2015; Mills et al., 2018; Walker et al., 2019; Clifton et al., 2020; Emberson, 2020) in this area. Due to effective environmental regulations and unusual situations such as COVID lockdowns, anth emissions continue to decrease there. For studies on Nr and O₃, attention should also be given to quantifying the impacts of multiple climatic factors as well as nonlocal air pollution sources such as those imported from upwind US regions, Canada, and the

65 stratosphere, which are partially controlled by the Bermuda High and other pressure systems (e.g., Colarco et al., 2004; Zhu et al., 2013; Ott et al., 2016; Rogers et al., 2020).

Previous global and regional modeling studies have shown that reproducing the observed warm-season Nr and surface O₃ levels in the US East is challenging (e.g., Fiore et al., 2009; Chai et al., 2007, 2013; Lapina et al., 2014; Huang et al., 2017a; 70 Lin et al., 2017). The estimated background O₃ therein, as well as the importance of its individual contributors, varies substantially among models. Often, the large model-observation mismatches in surface O₃ of up to tens of ppbv were not well explained or attributed mainly to the models' uncertain/outdated anth emission inputs. Some of these studies implemented advanced chemical data assimilation (DA) methods to reduce the errors in their predicted surface O₃ states by ~50% (Chai et al., 2007). They did not improve the mechanistic representations of O₃ related processes, which are of higher 75 policy-relevance and would lengthen the impacts of chemical DA since the model initializations/analysis times. The large uncertainty in model results limits our capability of understanding air quality over these regions and evaluating potential strategies to mitigate the air pollution impacts. High-resolution Earth system modeling with proper model parameterizations, up-to-date inputs, and comprehensive, process-based analysis aided by cross-disciplinary observations can help elucidate the various factors controlling Nr and O₃ (Fig. 1a) to better assist with assessing their environmental impacts from past to future.

80

This study is designed to support the International Global Atmospheric Chemistry-Tropospheric Ozone Assessment Report (TOAR) Phase II activity, which aims to further examine the distributions, temporal changes, and impacts of O₃ and its key precursors. A regional Earth system model is applied with updated parameterizations for selected land-atmosphere exchange processes (Section 2.1), running over the Northeast and Mid-Atlantic states for multiple years at 10 km horizontal resolution 85 that is considered to be able to better capture NO_x lifetime and budgets than coarser resolution systems (Li et al., 2023). The model is used together with multiplatform, multidisciplinary observations (Section 2.2) and a range of analysis methods (e.g., model evaluation and diagnosis, formal DA, and sensitivity simulations, Section 2.3) to help achieve the following specific goals: 1) to estimate Nr emissions from various anth and natural (e.g., soil NO and nitrous acid, HONO) sources, NO₂ surface concentrations and column densities, total and speciated Nr dry or/and wet deposition fluxes during 2018–2023, 90 with discussions on key anth and environmental/climatic drivers of their spatiotemporal variability during this period (Section 3.1); 2) to relate Nr and O₃ concentrations as well as their deposition fluxes during 2018–2023, in terms of spatiotemporal variability, reactions to environmental and biophysical stresses, and potential ecosystem impacts (Section 3.2); and 3) through three sets of case studies (Section 3.3), to discuss in detail about land-atmosphere exchange processes which have been understudied topics. Specifically, we demonstrate the capability of land DA to reduce the uncertainty in the 95 modeled land surface states, land-atmosphere exchange processes and atmospheric states at daily-to-interannual timescales; the impacts of controllable human activities such as irrigation on land surface and atmospheric fields and pollutants' ecosystem uptake; and the impacts of transboundary air pollution during selected extreme events on air pollutants' budgets

and ecosystem impacts. These case studies also help identify sources of model uncertainty before we draw conclusions and outline future directions for further advancements in related areas in Section 4.

100 2 Methods

2.1 Coupled modeling system and the baseline simulation

On a 10 km, 63 vertical layer Lambert conformal grid (Fig. 1b–c) from the subsurface to ~100 hPa, the NASA-Unified Weather Research and Forecasting model with online chemistry (WRF-Chem) simulations were conducted over the Northeast and Mid-Atlantic states for 2018–2023 growing seasons starting from 25 April of each year. The analysis of the baseline simulation was focused on May–June–July (MJJ) of 2018–2020, 2022, and 2023. MJJ falls within the plant growing and O₃ seasons when atmospheric Nr and O₃ most actively interact with ecosystems (Li et al., 2015; Clifton et al., 2020). Year of 2021 is not an emphasis in this paper partly due to the lack of reliable information to represent the COVID impacts on anth emissions for that year. The four-layer Noah-Multiparameterization (MP, Niu et al., 2011) land surface model (LSM) version 3.6 within the NASA Land Information System served as the land component of this modeling system, running with a sprinkler irrigation and the Community Land Model type of SM factor controlling stomatal resistance (i.e., β factor) schemes. Noah-MP was forced by the North American Land Data Assimilation System Phase 2 forcing data during the long-term (since 2000) offline spin-up. Noah-MP’s CO₂ forcings for 2018, 2019, 2020, 2022, 2023’s warm seasons were set to 410, 412, 415, 420, and 423 ppmv, respectively, based on measurements at the Mauna Loa Observatory and its nearby Maunakea Observatories for part of 2023 (https://gml.noaa.gov/webdata/ccgg/trends/co2/co2_mm_mlo.txt, last access: 12 January 2024). This advanced Noah-MP’s default setup in terms of appropriately representing the global CO₂ growth rates of 2–3 ppmv year⁻¹ for recent years (https://gml.noaa.gov/ccgg/trends/gl_gr.html, last access: 12 July 2024). Ignoring the spatial and (intra)seasonal variability in CO₂ of up to tens of ppmv over the study region (Karion et al., 2020) may have introduced only small uncertainty in photosynthesis and deposition modeling according to independent model sensitivity analysis in which CO₂ forcings were perturbed (e.g., Sun et al., 2022). The land use/land cover (LULC) and soil type inputs of Noah-MP were based on the 20-category International Geosphere-Biosphere Programme-modified Moderate Resolution Imaging Spectroradiometer (MODIS, Fig. 1b) and the 16-category State Soil Geographic (Fig. S1) datasets, respectively. Crop-type and irrigation map/fraction information required by the irrigation scheme came from Monfreda et al. (2008) and Salmon et al. (2015), respectively, the latter of which (Fig. 1c) incorporated MODIS information.

125 Major atmospheric and land model physics as well as chemistry schemes were configured in similar ways to those in Huang et al. (2022). The photosynthesis-based dry deposition approach recommended in Huang et al. (2022) and a number of other previous dry deposition studies cited therein was applied to most gaseous species. No change was made to sulfur dioxide dry deposition approach (Erisman et al., 1994) for this study. The modeled wet deposition fluxes were also evaluated and discussed in this work. In replacement of the metric-based approach in Huang et al. (2022), O₃ vegetative impacts were

130 dynamically modeled by applying two separate factors to photosynthesis and stomatal conductance rates (Lombardozi et al., 2015) that are calculated in Noah-MP. These factors are land cover-dependent functions of O₃ uptake cumulated during growing season when leaf area index (LAI) exceeds 0.5. To account for the ability of plants to detoxify O₃, O₃ fluxes were only accumulated when they exceeded a threshold of 1.0 nmol O₃ m⁻² s⁻¹. As demonstrated in previous offline (Lombardozi et al., 2015) and online (Li et al., 2016; Sadiq et al., 2017) modeling studies, dynamically modeling O₃ vegetative impacts
135 could help quantify the perturbations of O₃ to a variety of hydrological, ecological, and weather variables. Online-calculated biogenic emissions of O₃ precursors such as VOCs and Nr species in the simulations were adjusted to be more sensitive to multiple environmental stresses. Specifically, a drought adjusting factor γ_d was introduced in the Model of Emissions of Gases and Aerosols from Nature (MEGAN) biogenic isoprene emission calculations following the suggestions by Jiang et al. (2018), which depends on the β factor and the maximum carboxylation rate. The plant function type information needed for
140 MEGAN was converted from the annual European Space Agency Climate Change Initiative (ESA CCI) land cover product for 2018–2020, and the 2020 data from this product were also used for the years afterwards. The Noah-MP modeled LAI_v (i.e., LAI/Green Vegetation Fraction) feeds into MEGAN calculations. Soil emissions of NO were estimated largely based on the mechanism recommended by Hudman et al. (2012) and Simpson and Darras (2021), i.e., for dry and wet soils that are determined by a SM index (i.e., a function of SM, soil wilting point and field capacity), different sets of biome-based
145 emission coefficients (Steinkamp and Lawrence, 2011) and the standing Nr pool plus nitrogen input from deposition being adjusted by water-filled pore space θ (i.e., SM divided by porosity), soil temperature (Wang et al., 2021), and canopy reduction factor. The pulsing effects, which are small for this study area/season, were accounted for. Soil HONO emissions were also calculated online, scaled from soil NO emissions using biome-dependent factors specified in Table A1 of Rasool et al. (2019) that were partly adapted from Oswald et al. (2013). Nitrogen input from fertilizer was not included in the soil
150 emissions calculations to avoid double counting with agricultural emissions from the anth emission input to be introduced below. Oceanic natural NH₃ emissions were not included, which were estimated to have negligible impacts on Nr overland (Paulot et al., 2013). Lightning emissions were also calculated online and vertically distributed adopting the setup described in Huang et al. (2021) which was based on cloud-top-height-based parameterizations (Wong et al., 2013) and climatological intra-cloud to cloud-to-ground flash ratios. A passive lightning NO_x tracer was again implemented, that experienced
155 atmospheric transport but not chemical reactions. Aerosol direct, semidirect and indirect radiative effects were enabled.

Emissions from various anth source sectors came from the Copernicus Atmosphere Monitoring Service (CAMS) global inventory version 5.3, available at 0.1°×0.1° horizontal resolution with monthly and year-by-year variability. To account for COVID impacts, for 2020, grid- and sector-dependent factors (Dombia et al., 2021) were applied to adjust the emissions.
160 This CAMS inventory for the years after 2015 was developed by extrapolating the Emissions Database for Global Atmospheric Research version 5 based on the Community Emissions Data System version 2 trends and including emissions from ships as well as monthly variability that were estimated separately (Granier et al., 2019; Soulie et al., 2024). It's noted in Elguindi et al. (2020) and references therein that NO_x emissions for recent decades from an earlier version of CAMS

inventory do not notably differ from other bottom-up inventories over the US where more detailed information for emission
165 inventory developments are available. In contrast, top-down estimates diverge significantly due to uncertainty in the used
satellite NO₂ retrievals as well as the model representations of various atmospheric processes many of which are scale-
dependent. A clear understanding of the impact of background NO_x sources, including natural emissions, on constraining
NO_x emissions with satellite NO₂ data is urgently needed. The 0.1°×0.1°, version 2.6r1 of the Quick Fire Emissions Dataset
(QFED, Darmenov and da Silva, 2015), developed with the fire radiative power approach, was applied with plume rise
170 (Grell et al., 2011). QFED NO_x emissions over North America during 2012–2019 are in comparable magnitudes with other
widely-used fire emission datasets such as the Fire INventory from NCAR (FINN) while its NH₃ emissions are higher than
the estimates from other products (Wiedinmyer et al., 2023). Figure 2 presents the total anth and biomass burning (fire) NO_x
and NH₃ emissions averaged for each year's MJJ. Anth NO_x emissions are shown to decrease due to effective emission
controls (i.e., a -16.3% overall change from 2018 to 2023), except for slight increases along a few shipping lanes. They are
175 anomalously low in 2020 (~23.8% lower than 2018) largely due to reduced human activities during the COVID lockdowns.
The temporal changes in non-methane (NM) VOC emissions are relatively smaller, with the domain-mean in 2023 only ~6%
lower than in 2018. The total anth NH₃ emissions were growing in many places, most evidently over croplands as a result of
the rising agricultural soil and livestock emissions. The QFED-based fire NO_x and NH₃ emissions were generally increasing,
reaching their highest in 2023.

180

Daily reinitialized atmospheric initial conditions (ICs) and boundary conditions (BCs) were downscaled from the 3-hourly,
32 km North American Regional Reanalysis dataset. A set of the 6-hourly Community Atmosphere Model with Chemistry
(CAM-Chem, for 2018–2020, 0.9°×1.25°/56 vertical levels) and Whole Atmosphere Community Climate Model (WACCM,
beyond 2020, 0.9°×1.25°/88 vertical levels) simulations that also ingested QFED fire information served as the chemical
185 BCs of the WRF-Chem baseline simulation because of its higher completeness of chemical species, and for WACCM, its
availability for very recent years compared to chemical reanalysis products which are likely to be more accurate. The
chemical BC models' stratospheric O₃ tracer fields also supported our multi-year analysis and a case study (Section 3.3.3).
From 2018 to 2023, the lower free tropospheric O₃ in MJJ first rose by up to 4 ppbv, and then dipped down by up to 4–6
ppbv before rising again (Fig. 3a). The interannual variability in lower free tropospheric O₃ and its precursors upwind of the
190 eastern US, as well as the synoptic wind fields that shifted from westerly in 2018–2022 to northwesterly in 2023 (Fig. 3c),
play critical roles in controlling the modeled large-scale O₃ patterns and their temporal changes. Ozone transport from the
stratosphere more strongly influenced the lower free tropospheric O₃ over the southern part of our domain in 2023 than in
2018 by up to 4 ppbv (Fig. 3a–b). Although the stratospheric air influences on surface O₃ were diluted to no more than a few
ppbv (Fig. S2), the challenges regional models experience in reproducing their magnitudes and interannual variability may
195 introduce uncertainty to the estimated surface O₃ changes.

2.2 Observations

2.2.1 Chemical observations from satellites, aircraft, and ozonesondes

The TROPospheric Monitoring Instrument (TROPOMI) on board the Copernicus Sentinel-5 Precursor satellite launched in 2017 provides trace gas and aerosol measurements at daily global coverage since April 2018, with ascending node ~13:30 local time overpasses. It has much finer resolutions (i.e., $3.5 \times 5.5 \text{ km}^2$ at nadir since August 2019, and $3.5 \times 7 \text{ km}^2$ before then), a wider spectral range and higher signal-to-noise ratio per ground pixel than its predecessors. TROPOMI data have demonstrated their robustness in studying air pollution from numerous source sectors (e.g., land and water traffic, power plants, oil, gas and other industries, biogenic and fire) in greater detail (e.g., Georgoulas et al., 2020; van der Velde et al., 2021; Griffin et al., 2021; Goldberg et al., 2021; Dix et al., 2022). In this study, the gridded ($0.02^\circ \times 0.02^\circ$) monthly and daily level 2 TROPOMI tropospheric vertical column NO_2 data were analyzed together with WRF-Chem fields to help understand the temporal changes in column NO_2 . The gridded ($0.05^\circ \times 0.05^\circ$) monthly TROPOMI formaldehyde (HCHO) tropospheric vertical columns (De Smedt et al., 2021) were also used to calculate HCHO/ NO_2 ratios to help determine O_3 chemical regimes over the study area. The TROPOMI-based HCHO/ NO_2 ratios were supplemented by those derived from the gridded ($1 \text{ km} \times 1 \text{ km}$) NO_2 and HCHO data collected on selected days of 2018 over New York City and the Long Island Sound by two similar airborne instruments (Judd et al., 2020) Geostationary Trace gas and Aerosol Sensor Optimization (GeoTASO) and GEO-CAPE Airborne Simulator (GCAS).

Additionally, to help identify and attribute air pollutants during highly polluted events in 2023 (Section 3.3.3), the Joint Polar Satellite System-1 Cross-track Infrared Sounder (JPSS-1/CrIS, with descending/ascending nodes of ~1:30/13:30 local time) O_3 , carbon monoxide (CO), and PAN level 2 daily summary data provided by the Tropospheric Ozone and Precursors from Earth System Sounding project, were analyzed. The analysis of these extreme events was also supported by eight ozonesondes launched from the Virginia Commonwealth University Rice Rivers Center (RRC, 37.33197°N , 77.20842°W) during the inaugural edition of NASA Student Airborne Research Program (SARP)-East campaign in summer 2023 along with model results and ground-based observations (Section 2.2.3).

220

2.2.2 Satellite SM and precipitation products

To characterize drought conditions and their temporal variability, which interact with atmospheric chemistry, NASA's L-band Soil Moisture Active Passive (SMAP) 9 km enhanced surface (first 5 cm belowground) SM (SSM) data version 5 were utilized, as well as the version 7 of daily precipitation data from the NASA-JAXA Global Precipitation Measurement (GPM) produced at $0.1^\circ \times 0.1^\circ$ resolution using the Integrated Multi-satellitE Retrievals for GPM-Final run algorithm. Despite the different sampling strategies and retrieval algorithms of SMAP and GPM, interannual variability in the drought conditions indicated by these SSM and precipitation data are qualitatively consistent (Fig. 4), which are also consistent with information from independent sources such as the North American Drought Monitor (<https://droughtmonitor.unl.edu/NADM>, last access:

225

12 July 2024; see Table S1 and Fig. S3 for further analysis and discussions). In addition to rainfall, irrigation water and other
230 elements relevant to water and energy balances can also impact the variability in SSM which has feedback to the regional
precipitation patterns. The wide range of the SMAP SSM from <0.2 to $>0.5 \text{ m}^3 \text{ m}^{-3}$ and its interannual differences which
often exceed $0.1 \text{ m}^3 \text{ m}^{-3}$, indicate the diverse SM regimes (i.e., dry, transitional, and wet) and therefore spatially and
temporally varying land-atmosphere coupling strengths (Seneviratne et al., 2010, and references therein). The varying SSM-
235 temperature coupling strengths were determined based on WRF-Chem results, with support of the $0.25^\circ \times 0.25^\circ$ European
Centre for Medium-Range Weather Forecasts Reanalysis version 5 (ERA5) surface air temperature field. In a case study
(Section 3.3.1), SMAP SSM data were assimilated into the Noah-MP LSM to improve the land ICs of WRF-Chem, and
further, the modeled weather and atmospheric chemistry fields.

2.2.3 Ground-based observations

240 Hourly surface ultraviolet absorbance O_3 observations from the US EPA's Air Quality System (AQS, a major source of the
TOAR database, last update in August 2024) were used to support the quantification of O_3 temporal variability and model
evaluation. The AQS NO_2 observations, which have poorer spatial coverage than their O_3 data, were also examined to help
qualitatively understand surface NO_2 variability. These AQS NO_2 measurements made using the chemiluminescence
detection with catalytic conversion are known to be positively biased by up to 50% due to NO_z (NO_y - NO_x) interferences
245 (e.g., Dunlea et al., 2007). Speciated aerosol measurements offered by the Clean Air Status and Trends Network
(CASTNET) and AQS, CASTNET HNO_3 , the National Atmospheric Deposition Program (NADP)/Ammonia Monitoring
Network (AMoN) NH_3 observations, as well as the NADP/National Trends Network (NTN) wet deposition fluxes and
precipitation data, were used to infer or directly evaluate WRF-Chem's deposition performance. Deposition datasets from
other studies, some of which integrated surface or/and satellite observations with other models (e.g., Schwede and Lear,
250 2014; Fu et al., 2022; Rubin et al., 2023), will be referred to in the discussions.

Additional datasets for selected time periods were used in DA case studies to help interpret and validate the model results
(Section 3.3.1). These include gauge-based precipitation data and SSM measured using HydraProbe sensors at Harvard
Forest, Massachusetts (42.53523°N , 72.17393°W) and a US Climate Reference Network (CRN) site in Millbrook, New
255 York (41.786°N , 73.74°W) during the July 2022 SMAP validation experiment (SMAPVEX22); and surface air temperature
observations in July 2018 and 2022 from the National Centers for Environmental Prediction (NCEP) Global Surface
Observational Weather Data product.

2.3 Case studies and sensitivity simulations

Temporal variability of Nr and O_3 concentrations and fluxes at subregional-to-local scale are partially driven by hydrological
260 variability which can be influenced by both precipitation and human activities such as irrigation. Two sets of modeling and
DA case studies (Sections 2.3.1 and 2.3.2) were conducted to show that the modeled land surface states, such as SM, can be

improved via land DA and/or updating the model's irrigation schemes, which further impacts the modeled land-atmosphere exchange processes and atmospheric fields.

2.3.1 Effects of SM DA on modeled NO₂ and O₃

265 For this case study, SMAP morning-time (~6 am local time) SSM data were bias-corrected via matching the means and standard deviations of SMAP and Noah-MP SSM monthly climatology. The bias-corrected data were then assimilated into the Noah-MP LSM using a 40-member ensemble Kalman filter approach to adjust WRF-Chem's land ICs during July 2018 and July 2022. Meteorological forcing (precipitation, short- and longwave radiation) and state (Noah-MP SM) perturbation attributes were set up largely based on Kumar et al. (2009) recommendations for the Noah LSM, and the input observation error standard deviation was set to be 0.04 m³ m⁻³ according to the SMAP data quality requirement. Through this experiment we evaluate whether and to what extent can satellite SM DA improve the day-to-day (i.e., before and after a precipitating event during the SMAPVEX22 campaign when in situ SSM data were also collected near the SMAP morning overpassing times) and interannual variability (i.e., July 2018 and July 2022) of Noah-MP SM, even in dense vegetation regions such as the eastern US where satellite SM retrieval is generally more challenging. How the adjustments to Noah-MP land surface states by DA impacted the modeled atmospheric fields was also quantified.

2.3.2 Irrigation impacts on O₃ vegetation uptake and Nr deposition

Using flux-based O₃ metrics derived from model outputs, recent studies (Mills et al., 2018; Huang et al., 2022) estimated that the negative impacts of ground-level O₃ on crop yields are particularly large in humid irrigated and rainfed agricultural lands, where the plants' stomatal uptake of O₃ is significant. The global-scale coarse-resolution analysis for 2010–2012 by Mills et al. (2018), which was based on O₃-flux metrics, also estimated that irrigation promotes the O₃ impacts on wheat production by up to ~10%. To dynamically evaluate in detail the irrigation impacts on land surface and atmospheric fields as well as the estimated O₃ and Nr ecosystem impacts across our study area for recent years, WRF-Chem simulations were conducted with three sets of irrigation configurations, defined as (a, b, c) below, and for each of these three scenarios, two simulations were conducted with and without O₃ vegetation impacts:

- a) Full irrigation (baseline): Sprinkler irrigation occurs in the morning when rootzone SM drops below 50% of field capacity;
- b) Reduced irrigation: Sprinkler irrigation occurs in the morning when rootzone SM drops below 25% of field capacity, and the estimated irrigation water usage for this scenario is ~1/6 of the full-irrigation scenario for irrigated areas south of ~37°N in our domain;
- 290 and c) Irrigation option was completely disabled.

This sensitivity analysis is focused on 21–30 June 2022, when irrigated fields in the Carolinas that grow mostly O₃-sensitive crops were under stress according to the Vegetation Drought Response Index produced by the National Drought Mitigation Center (Fig. S4). This region also encompasses Nr deposition hotspots that have been experiencing critical load (CL) exceedances (i.e., the amount of Nr deposition exceeds the CL threshold, the point above which deposition could harm

295 sensitive ecosystems). For this period, irrigation water consumption under the full-irrigation scenario may be higher than normal, and the estimated surface fluxes under reduced- and no-irrigation scenarios may be particularly smaller than usual and more strongly constrained by SM.

2.3.3 Impacts of transboundary pollution on weather, air quality and ecosystems

300 The Northeast and Mid-Atlantic US air quality is regularly affected by pollutants emitted or/and formed in upwind US states. Actions have been taken to tackle cross-state air pollution such as using the Cross-State Air Pollution Rule framework (<https://www.epa.gov/Cross-State-Air-Pollution/overview-cross-state-air-pollution-rule-csapr>, last access: 12 January 2024). However, with the US EPA's "Good Neighbor Plan" being put on hold by the Supreme Court (<https://www.epa.gov/Cross-State-Air-Pollution/good-neighbor-plan-2015-ozone-naaqs>, last access: 12 July 2024), downwind US states may continue to
305 face difficulties in complying with the 2015 O₃ National Ambient Air Quality Standards due to the upwind states' pollution impacts. Periodically, distant sources including Canadian wildfires and O₃-rich stratospheric air also travel to the northeastern and Atlantic states. Satellite and in situ observations are powerful in detecting such episodic events that occur more frequently in recent years, assisting with early warnings and early actions. To help quantify the impacts of such extreme events, as well as other upwind air pollution sources, on weather, air quality and ecosystems during 13–16 June
310 2023, two WRF-Chem sensitivity simulations were conducted and analyzed together with the baseline simulation and multiplatform observations. Clean chemical BCs were applied in one of these sensitivity simulations, and WACCM running with the FINN fire emission input served as the chemical BCs of the other WRF-Chem sensitivity simulation named "Sen". Fire emission is identified as one of the most important configurations in global wildfire modeling (e.g., Veira et al., 2015).

3 Results and discussions

315 3.1 Nr emissions, concentrations, and deposition fluxes during 2018–2023

The modeled soil NO and HONO emissions vary strongly with SM as well as soil temperature that can be impacted by SM. Even without land DA the model fairly well reproduced the large-scale spatial gradients and interannual variability of soil wetness (Figs. 4a and S5). Soil emissions exhibit notable monthly variations, with multi-year June- and July-mean values ~11% and ~59% higher than the May-mean, respectively, associated with overall warmer and drier conditions. These
320 monthly variations, together with the ~8% and ~18% multiyear June-May and July-May mean differences in anth+fire emissions as well as modeled surface and column NO₂ fields, help interpret the higher TROPOMI and AQS NO₂ on warmer months over many rural areas, especially those near high-temperature agricultural regions (Fig. S6), a point Goldberg et al. (2021) also highlighted. The maxima and minima of MJJ soil emissions are shown in 2020 and 2018, respectively, and the interannual variability of soil emissions roughly anti-correlates with that of SM, with correlation coefficient r ranging from
325 -0.63 to -0.40 ($p < 0.01$; Fig. 5a,c). For most years, the estimated MJJ-mean soil NO and HONO emissions are particularly high in warm and/or dry areas including parts of the Carolinas, Virginia, New York, Michigan, and Canada's Ontario, where their contributions to the total soil+anth+fire NO_y emissions persistently exceeded 30% (Fig. 5a–b). Based on a global

atmospheric chemistry model with a similar soil emission scheme, previous estimates of the soil NO emission contributions to column NO₂ for this area were minor compared to other US regions in 2005 (i.e., <15% uniformly, Vinken et al., 2014),
330 when anth NO_x emissions were >25% higher than in 2018 according to the CAMS inventory and other estimates. Owing to the overall declining US anth emissions and the changing climate, soil emissions play an increasingly important role in controlling Nr, and further, O₃ air quality, in this area. Accordingly, the needs to properly parameterize soil emissions and accurately model soil environments (e.g., SM, soil temperature, pH) have been growing stronger which could greatly benefit from laboratory and field experiments.

335

Despite the increasing anth NH₃ and fire Nr emission trends (Section 2.1) and the abovementioned interannual variability in soil NO and HONO emissions, the total Nr emissions as well as surface NO_y emissions that contributed to >50% of the total Nr emissions show decreasing year-to-year changes during 2018–2023 except for the dip in 2020 that is mainly attributable to the COVID lockdowns (Fig. 6a). Closely linked to such temporal changes in NO_y emissions, that in many areas
340 overwhelm the effects of slower NO₂ and NO_y dry deposition (Fig. S7 and later discussions), the modeled column and surface NO₂ both display downward changes since 2018, with their lowest values occurring in 2020 (Figs. 6b and 7). From 2018 to 2023, on average, column and surface NO₂ dropped by 15–20%. Impacted by the decreasing NO₂, HCHO columns overall demonstrate a few percent slower year-to-year changes than NO₂ (Fig. S8), in large part because of less significant NMVOC emission changes (Section 2.1). Impacted mostly by shipping and lightning emissions as well as North American
345 pollution outflows, the amount of NO₂ above the ocean is lower than overland. Early afternoon (19 UTC, local standard time +5 or +6, near TROPOMI overpassing times) surface and column NO₂ are ~44% and ~29% lower than their daytime averages (13–24 UTC, roughly the sampling times of geostationary missions such as the Tropospheric Emissions: Monitoring of Pollution, TEMPO, and the anticipated Geostationary Extended Observations). The stronger subdaily variability in surface NO₂ than in column NO₂ reflects the impacts of photochemistry and evolution of planetary boundary
350 layer on the rapidly changing vertical distributions of chemicals throughout the daytime which have also been demonstrated in Huang et al. (2017b) and other studies with aircraft observations. Dependent strongly on convection, lightning NO emissions show high variations from year to year in terms of locations and magnitudes, having larger impacts on free-tropospheric and column-average NO₂ than surface NO₂ (Fig. S9).

355 The column NO₂ spatiotemporal variability based on WRF-Chem and TROPOMI greatly resemble one another (Fig. 7a–b), and larger model-TROPOMI discrepancies are seen over the areas possibly influenced by lightning NO emissions and transboundary pollution where both model and retrieval errors may be large. The interannual variations in such pollutant sources aloft may also explain the different interannual variability in surface and column NO₂ for some locations and years. AQS NO₂ data, although sparsely distributed and positively biased, qualitatively confirmed the model-suggested year-to-year
360 changes in surface NO₂ (Fig. S10).

Drought conditions, as well as the opposite directions of NO_y and NH_3 emission and concentration changes, helped shape the interannual variability in the total Nr deposition fluxes (Fig. 8a). Overland, the modeled Nr wet deposition fluxes often contributed to nearly or lower than 30% of the total Nr deposition. These contributions are smaller than earlier estimates for this area (e.g., <60% in Tan et al., 2018, where wet deposition based on 11 global models was overestimated), due in part to WRF-Chem wet deposition being underestimated referring to the NADP/NTN measurements (Table S2 and Fig. S11). This underestimation in wet deposition can be attributed to known limitations in the WRF-Chem wet deposition scheme (Ryu and Min, 2022; Yao et al., 2023). The underestimated model precipitation rates and inaccurate model precipitation patterns on event-to-seasonal scales (Figs. 4b, S5, and S11; Section 3.3.1 case study), as well as observation representation errors, also have caused the negative biases in wet deposition fluxes and the positive biases in aerosol concentrations especially for NH_4 and NO_3 (Figs. S11–S14). Such precipitation biases in WRF have also been reported in previous studies, and they can indirectly impact dry deposition modeling.

Dry NO_y deposition fluxes decreased evidently (i.e., by 5–16% overall and >50% in some populated areas) whereas NH_x dry deposition fluxes show up to $\pm 3\%$ of overall interannual variability and rose by >20% over certain agricultural lands (Fig. S15) where NH_3 emissions have been climbing up. Due to not applying a bi-directional approach (Zhang et al., 2010; Massad et al., 2010; Pleim et al., 2019), these NH_3 fluxes may be overestimated over source regions by a few percent (Zhu et al., 2015; Liu et al., 2020a), contributing to the model's minor negative NH_3 biases relative to the NADP/AMoN data (Table S2 and Fig. S13). Nevertheless, the contrasting directions of change in NO_y and NH_x deposition fluxes as well as the importance of NH_x deposition in total deposition corroborate results from other studies for earlier periods (e.g., Schwede and Lear, 2014; Li et al., 2015; Jia et al., 2016; Geddes and Martin, 2017; Liu et al., 2020b, and references therein). With several percent of interannual differences in flux partitioning (Fig. 8b–c), in all years' MJJ, HNO_3 and NH_3 contributions (>35%) dominated in the Nr dry deposition fluxes. NO dry deposition is negligible due to extremely high surface resistance and in figures is combined with NO_2 into NO_x fluxes, that contribute to 12–15% of Nr dry deposition fluxes. Unlike most other species, surface resistance of HNO_3 is nearly zero, whose dry deposition variability is therefore driven dominantly by aerodynamic resistance and quasi-laminar sublayer resistance and responds differently to drought conditions than the other Nr species and O_3 (Section 3.2). The modeled HNO_3 daytime dry deposition velocities over most forested areas fall within 4–8 cm s^{-1} , close to the measurements reported in literature for similar land cover types in the eastern US (e.g., Nguyen et al., 2015). These are ~a factor of 10 higher than the dry deposition velocities of NO_2 and PAN, similar to the results in Wu et al. (2011) based also on a photosynthesis-based dry deposition model and the flux measurements summarized by Delaria and Cohen (2023).

Many global models have provided their estimates of total and speciated Nr deposition fluxes for previous decades (e.g., Dentener et al., 2006; Paulot et al., 2018; Tan et al., 2018; Rubin et al., 2023). Here, our regional model results present more details which could be beneficial for estimating CL exceedances on relatively smaller spatial scales. They are overall of a

lower magnitude, reflecting the impacts of the declining NO_y and Nr emissions which are anticipated to continue into the coming decades. This may also be attributed to the impact of the changing climate and the model uncertainty relevant to scales, deficits in deposition schemes and inputs as well as uncounted deposition of certain organic Nr species due to our chosen chemistry and aerosol schemes. Possibly also for these reasons, a little over 50% of the surface Nr emissions were estimated to be removed via deposition in this area for all years (Fig. 6a), slightly lower than the estimates in previous modeling studies.

Comparing our WRF-Chem Nr deposition fluxes to the CL thresholds in Simkin et al. (2016) for herbaceous plants that range from 7.4 to 19.6 $\text{kg ha}^{-1} \text{a}^{-1}$, from 2018 to 2023, the high likelihoods of CL exceedances in Pennsylvania dropped whereas those in parts of North Carolina may have remained high. The Nr deposition fluxes stayed below these CL thresholds over most of the northern forests, a region where primary productivity has been determined to be nitrogen-limited (Du et al., 2020) and can be highly sensitive to the interannual variability in Nr deposition (Fig. S16). The empirical CL thresholds of $>3\text{--}8 \text{ kg ha}^{-1} \text{a}^{-1}$ for the eastern US forests in Pardo et al. (2011) are higher than the modeled Nr deposition fluxes over the forests in New England states and West Virginia whereas for the other forests roughly close to or lower than the modeled. These results help explain the findings in Horn et al. (2018) that tree growth and survival have increasing and flat-to-slightly-decreasing relationships with Nr deposition for New England/West Virginia forests and other eastern US forests, respectively. For lichen, WRF-Chem suggests that widespread CL exceedances occurred throughout the study period, according to the static CL thresholds of 3.5, 3.1, 1.9, and 1.3 $\text{kgN ha}^{-1} \text{a}^{-1}$ for total species richness, sensitive species richness, forage lichen abundance, and cyanolichen abundance, respectively (Geiser et al., 2019). Note that these lichen CL thresholds are likely to be conservative for the eastern US as they were derived partially from biased model deposition fields, and further assessments on the uncertainty of these thresholds are necessary.

3.2 Spatiotemporal variability of Nr and O_3 concentrations and deposition fluxes

The interannual, day-by-day and subdaily variability in HCHO/NO_2 ratios derived from TROPOMI and airborne GCAS and GeoTASO data indicates the variable photochemical environments driven by the changing meteorology and emissions, but, as noted in a number of prior studies (e.g., Duncan et al., 2010; Jin et al., 2017; Tao et al., 2022; Souri et al., 2023), can also be affected by retrieval uncertainty and several other types of errors. Yet, they indicate that, much of the study area belong to NO_x -sensitive or transitional chemical regimes during 2018–2023 (i.e., HCHO/NO_2 higher than empirical thresholds of 2–4, Fig. 9) except very few megacities such as the Greater New York City and Toronto, Canada, and for those urban regions, O_3 formation continues the trends of turning sensitive to NO_x .

Largely explainable by the changing NO_y emissions and NO_x -sensitive chemical regimes, the spatial patterns of the modeled interannual differences in column NO_2 and surface O_3 concentrations roughly resemble one another. Both NO_2 and O_3 display downward changes over the majority of terrestrial areas whereas the opposite direction of changes over the Atlantic

430 Ocean (Figs. 7b and 10a). In more than half of the terrestrial model grids, the interannual variability of 19 UTC NO₂ columns and daytime surface O₃ are moderately correlated ($r > 0.6$), with the r value of 0.57 averaged across all overland grids and 0.92 for grids where the p values of the correlation tests are lower than 0.05. Fig. 11 indicates the connection between early afternoon (19 UTC) NO₂ columns and daytime surface O₃ as well as its dependency on column HCHO/NO₂ ratios. Daytime surface O₃ concentrations exhibit the most robust spatial correlations with early afternoon NO₂ columns in
435 2020 ($r = 0.62$, versus 0.54 for all years, Fig. 11), when the domain-wide median and mean HCHO/NO₂ ratios are larger than the other years' by at least 0.5. These point to a potential of inferring surface O₃ variability from high-quality remote sensing NO₂ and HCHO column data across this area.

The reduction in NO_y emissions contributed to the domain-average changes in median (-0.7 ppbv) and mean (-1.0 ppbv)
440 daytime surface O₃ concentrations overland from 2018 to 2023, which are much smaller than that in 95th% O₃ (by -3.5 ppbv). The lowering NO_y emissions also resulted in less titration, and consequently, the slightly increased 5th% O₃ (by 0.3 ppbv). Such modeled general directions of O₃ temporal changes in this area over the past ~5 years are qualitatively consistent with Cooper et al. (2012) for springs and summers of 1990–2010 as well as follow-on studies (Simon et al., 2015; Lin et al., 2017; Gaudel et al., 2018) and the US EPA's periodically-updated O₃ trend summary (<https://www.epa.gov/air-trends/ozone-trends>, last access: 12 July 2024). The model captured the COVID-induced daytime surface O₃ reductions in 2020 (i.e.,
445 overland, ~0.8 ppbv lower than in 2019 on average) that have also been reported in numerous independent studies (e.g., Keller et al., 2021; Steinbrecht et al., 2021; Putero et al., 2023). The interannual variability of imported O₃ and its precursors from other regions, as well as the interconnected environmental and plant physiological conditions (e.g., via soil-vegetation-atmosphere interactions whose strengths vary in space and time) modulated biogenic VOC emissions, deposition, chemical
450 reactions, transport and mixing, also drove the O₃ changes on regional-to-subregional scales.

The spatial patterns of WRF-Chem modeled surface O₃ broadly match the AQS observations for most of the years (Fig. 10), with root-mean-square errors (RMSEs) ranging from 4.0 to 6.5 ppbv which are significantly lower than the magnitudes of tens of ppbv in many earlier modeling studies for the similar regions. The better performance may have substantially
455 benefited from the advancements in model parameterizations and the updated anth emission inputs. Although WRF-Chem surface and column NO₂ temporal changes agree well with the observed, the model struggled to capture the observed deviations of surface O₃ in 2023 from previous years, likely due to its failure in representing the particularly strong influences of stratospheric O₃ or/and other extra-regional sources on (near-)surface O₃ in 2023 (Figs. 3b and S2). Later in a case study, the dependency of WRF-Chem O₃ performance on how well transboundary pollution as well as regional climatic
460 conditions and their driving processes are represented in the model will be investigated further.

Similar to dry deposition of Nr species and conclusions from Huang et al. (2022), the spatiotemporal variability of O₃ dry deposition velocities is closely linked with land cover types, environmental and vegetation conditions, with their highest

daytime-average values ($v_{d,o_3} > 1.0 \text{ cm s}^{-1}$) seen over moist forests and >30% lower daytime-average values over croplands
465 experiencing drier conditions (Figs. S7 and S15). Cumulative stomatal O_3 uptake (CUO), a recommended metric for
assessing the potential O_3 vegetation impact, that is affected by stomatal conductance, boundary layer resistance, and surface
 O_3 levels, appears also high over the croplands in Ohio and Indiana ($\sim 40 \text{ mmol m}^{-2}$) where surface O_3 concentrations are
high while much lower over drier croplands in the Carolinas ($< 30 \text{ mmol m}^{-2}$). Except for regions influenced by the wetter-
than-normal conditions or/and increasing surface O_3 concentrations, the CUO fields show declining trends (i.e., overall
470 dropped by $\sim 10\%$ from 2018 to 2023). Our results are qualitatively consistent with those in Clifton et al. (2020) for the
northeastern US, where based on a global model, stomatal O_3 uptake cumulated through MJJ 2010 with no detoxification
threshold was estimated to be $\sim 35 \text{ mmol m}^{-2}$. Their modeled flux was projected to decrease under the Representative
Concentration Pathways 8.5 future scenario under which soil may be drier than present day conditions over the eastern US
(Cook et al., 2020). As indicated in Fig. 12a, our modeled CUO values are higher over croplands and forests than shrub/grass
475 averagely and more spatially variable. These CUO fluxes display clearer trends in most grids than the total Nr deposition
fluxes, due to NO_y and NH_x deposition fluxes having competing directions of changes through the past years (Figs. 8b–c and
S15). The potential impacts of Nr deposition are strongest and weakest on croplands and water, respectively (Fig. 12b).

3.3 Three case studies

480 3.3.1 Land DA

As indicated by GPM, SMAP, and in situ observations collected at Harvard Forest and the CRN-Millbrook site during the
SMAPVEX22 campaign, a precipitating event associated with a frontal passage occurred from late 13 July to early 14 July
2022 causing sharp increases in SSM around 14 July in Massachusetts (by $> 0.06 \text{ m}^3 \text{ m}^{-3}$) and parts of the eastern New York
(by $\sim 0.02 \text{ m}^3 \text{ m}^{-3}$) where surface O_3 dropped abruptly by up to 30 ppbv (Figs. 13a and S17). Baseline simulation without DA
485 failed to reproduce this strong daily SSM variability at site-to-regional scales (Fig. 13b). After enabling the SMAP DA,
Noah-MP SSM in Massachusetts and the eastern New York increased remarkably on 14 July (Fig. 13c), better matching the
observed quantities. Along the southern New York-Connecticut as well as the northern New York-Vermont borders, the
slightly drier conditions on 14 July are also better represented in Noah-MP with the implementation of SMAP DA (Fig. 13a–
c). The enhancements in soil wetness resulted in a bit cooler surface soil/air, thinner atmospheric boundary layer, suppressed
490 biogenic VOC and soil NO_y emissions as well as O_3 formation while deposition accelerated. Lightning emissions were also
sensitive to the DA-induced SM changes. Consequently, above many Connecticut River watershed areas, WRF-Chem NO_2
columns dropped (Fig. 13e–f). Due to increased upwind pollution contributions whereas weakened local emissions and
production, both enhancements and reductions by up to ~ 4 ppbv in daytime surface O_3 levels (not shown in figures) are
found in the New England region ($40.5\text{--}43.1^\circ\text{N}$, $70.0\text{--}74.0^\circ\text{W}$). Across the New England region, WRF-Chem daytime
495 surface O_3 performance for 14 July was improved in 31 out of 50 of the model grids where AQS data were available, with
the largest improvement of nearly 2 ppbv. It is also highlighted that the various processes SM can impact help shape the
vertical profiles of NO_2 and other chemical species, a critical ancillary data for calculating the air mass factor that is needed

to convert slant columns to vertical columns in satellite retrievals (Lorente et al., 2017) and derive averaging kernels (AKs, Eskes and Boersma, 2003). At Harvard Forest, the vertical distributions of NO₂ as well as their responses to SMAP DA changed rapidly during this event (Fig. 13g–h), despite the minor change in NO₂ column. It is suggested that cautions are taken when attributing the mismatches between TROPOMI and models (with AKs, that indicate lower TROPOMI sensitivity towards the surface) over the scenes where NO_x near the surface and aloft may both be significant. Also, productions, interpretations, and applications of satellite NO₂ retrievals could benefit from evaluating and tuning their model-based *a priori* profiles with in situ measurements of NO₂ vertical distributions under various environments.

505

Figure 14a–c illustrates that, on a larger timescale, SMAP DA effectively narrowed the Noah-MP wet biases in July 2022–July 2018 SSM differences in Canada’s Ontario (croplands) as well as the dry biases in Virginia (forests) that may have resulted from inaccurate representations of meteorological drought conditions. WRF-Chem weather fields, biogenic VOC, soil NO_y and lightning emissions, and deposition processes all responded to the DA-induced changes in the model’s land ICs. The July 2022–July 2018 differences of WRF-Chem NO₂ columns and surface O₃ over these regions became closer to (by as high as ~50% and >4 ppbv, respectively) what TROPOMI and AQS observations indicate (Fig. 14d–i). Notably, the SMAP DA flipped the sign of surface O₃ interannual differences over the northern Virginia, for which region the DA had strong impacts on the modeled surface O₃ in both July 2018 and July 2022 (Fig. S18). The remaining modeled-observed NO₂ and O₃ discrepancies over some of the northern states and coastal North Carolina, which are highly correlated because of the dominating NO_x-limited regime, can also be explained by uncertainties in the model’s chemical BCs and wind fields.

515

These analyses demonstrate that microwave satellite SM DA can improve the modeled SM dynamics at daily-to-interannual timescales. Similar findings were previously reported by Draper and Reichle (2015) where SM from the X-band (sensitive to top ~1 cm soil) Advanced Microwave Scanning Radiometer–Earth Observing System was assimilated at only four sites, but not on regional scales for forested regions where SM retrievals have been considered challenging and need validation. It is also shown in this work that the DA adjustments to LSMs’ SM fields can positively impact weather and chemistry fields from their coupled atmospheric models, benefiting our interpretations and prediction skills of air pollutants’ distributions and temporal changes which can in turn help advance satellite retrievals. It is important to note that SSM-atmosphere coupling strengths vary strongly in space and time, influenced by the evolution of local hydrological regimes. As 2022–2018 SSM and surface air temperature differences show strong negative correlations of -0.78 (Fig. S19), the land DA impacts on WRF-Chem’s atmospheric chemistry fields were in some part through adjusting the weather, as indicated in Figs. 14j–l and S18. For the times/locations that SSM and atmosphere coupling strengths are weak, land DA is anticipated to impact the modeled atmospheric chemistry fields mostly via the direct control of land surface on natural emissions and deposition.

520

525

530 3.3.2 Irrigation approaches

Based on the three sets of simulations representing full-, reduced-, and no-irrigation scenarios (Section 2.3.2), the impacts of irrigation on surface O₃ concentrations, CUO and O₃ injury to vegetation, as well as Nr deposition were quantified (Fig. 15). Across the domain, O₃ perturbs gross primary productivity more strongly (up to 20–30%) than transpiration (mostly <10%), and therefore reduces the vegetation water use efficiency. Its reductions to leaf biomass over the stressed irrigated lands in the Carolinas in late June 2022 are estimated to be <5% under all three scenarios. Under the limited- and no-irrigation conditions, O₃-induced crop yield losses were reduced over irrigated areas by up to ~2%, a result of lowered SM (Fig. S20) and deposition fluxes despite the enhanced soil/air temperatures, soil NO_y emissions and surface O₃ concentrations (by up to ~10 ppbv). This result supports and extends the findings from previous coarse-resolution modeling (Mills et al., 2018) and observational (Harmens et al., 2019) studies. The period-integrated O₃ stomatal uptake increased slightly outside of the irrigated land due to higher O₃ being transported away from the irrigated areas. Over/near the irrigated areas, the estimated total Nr deposition would also be lower under reduced- and no-irrigation scenarios by more than 50%, which would be below possible CL thresholds, as less irrigation would result in stronger atmospheric mixing and reduced SM although soil NO_y emissions would increase. These impacts on Nr deposition over most of the irrigated lands are important also according to Student's *t*-tests comparing the base and sensitivity simulations ($p < 0.05$). The impacts of irrigation on Nr deposition over non-irrigated areas are rather noisy and more intense than on O₃, where Student's *t*-tests comparing Nr deposition from different simulations gave larger-than-0.05 *p* values. These sensitivities away from irrigated lands still highlight the complex net effects of irrigation-induced changes in land surface and meteorological conditions on a group of species with substantially different properties undergoing various atmospheric processes.

Compared with long-term offline LSM simulations forced by independently produced O₃ data, evaluations of O₃ vegetation impacts using coupled modeling systems like WRF-Chem with land surface feedback to regional weather and atmospheric chemistry being accounted for are more realistic. Nevertheless, such approaches are hundreds of times more computationally expensive and may be subject to uncertainty from the atmospheric model. Survey- and satellite-based irrigation types and water use information, including wastewater use that may impact plant growth, nutrient supply and soil environments (Aman et al., 2018), direct stationary and/or airborne measurements of water, carbon, energy, air pollutants' concentrations and fluxes, as well as plant traits within and outside of irrigated areas for variable hydroclimatic conditions, would help evaluate and improve irrigation modeling and the model-based holistic assessments of irrigation impacts on regional environments that could assist with forming pollution mitigation and ecosystem adaptation strategies for future.

3.3.3 Transboundary pollution

Periodically, distant pollution sources make strong environmental impacts on the Northeast and Mid-Atlantic US states. For example, during the 2023 SARP-East campaign, JPSS-1/CrIS observed high O₃ and low CO on 13 June; and high O₃, CO, and PAN on the following days of the same week (Fig. 16) when elevated NH₃ columns and aerosol optical depths were also

observed from space by multiple instruments (not shown). These data suggest that long-range transported stratospheric air
565 and Canadian wildfire plumes reached the eastern US.

As indicated by the stratospheric O₃ tracer of the chemical BC model WACCM, the 13 June stratospheric intrusion event
associated with a frontal passage enhanced lower tropospheric O₃ by as high as 30–40 ppbv along the northeast corridor,
which helps explain the spike at ~700 hPa (>30 ppbv O₃ enhancement) in the SARP-East RRC ozonesonde profile for that
570 day (Fig. 17a–b). The WACCM-estimated stratospheric impact on surface O₃ in our WRF-Chem domain is only ¼–1/3 of its
impact on free tropospheric O₃ (Fig. S21), consistent with prior knowledge that stratospheric impacts on the US East are
often confined at higher altitudes while surface O₃ remains low (Ott et al., 2016). Thick Canadian wildfire plumes that
moved into the study region, dramatically enhanced O₃ spanning a wide altitude range (i.e., from >900 hPa to ~600 hPa)
above the RRC site on several days of that week (Fig. 17b). Under the strong influences of Canadian fires, O₃ in the US
575 outflows during that week was close to that in the air sampled ~two decades ago along the East Coast (Cooper et al., 2005).
Ozonesondes also indicate that air quality improved remarkably in the following week, with O₃ from the surface to ~700 hPa
nearly 40 ppbv lower (Fig. 17b).

The WRF-Chem baseline and “Sen” sensitivity simulations were evaluated with O₃ observations during 13–16 June 2023.
580 Overall, the baseline and “Sen” simulations moderately well reproduced the daytime surface O₃ patterns and diurnal cycles
observed at AQS sites during the events, with RMSEs of ~7 ppbv (Figs. 17c–k and S21). The negative mean biases of 1–2
ppbv in the modeled daytime peak O₃ (Fig. 17c) can be explained by the model’s incapability of accurately representing the
stratospheric O₃ influences. The choice of WACCM’s fire emission input had minor impacts on WRF-Chem daytime surface
O₃ averaged across the domain throughout the episode but enhanced/reduced WRF-Chem’s daily daytime surface O₃ by up
585 to ~10 ppbv on grid scale (Figs. S21–S22).

The extremely high transported background aerosols and their precursors due to Canadian wildfires, along with upwind US
pollution, interacted with meteorological and land surface fields (e.g., radiation, temperature, clouds, precipitation, and
surface wetness) that are relevant to evapotranspiration and photosynthesis (see also discussions on Asian anth pollution
590 impacts in Huang et al., 2020, and references therein), dry deposition velocity and wet deposition coefficient, and secondary
pollutant formation. The baseline and “Clean BC” cases together indicate that, although under highly polluted conditions,
dry deposition velocities are overall reduced (Fig. S23) and photochemistry activities are weakened, the period-integrated
CUO and mean total Nr deposition fluxes are enhanced as the excessive amount of imported pollution significantly elevated
surface O₃ and Nr concentrations (Fig. 18). During this period, daily O₃ stomatal uptake and the mean total Nr deposition
595 overland are ~2% and ~26% higher than their 2023 seasonal-mean values, respectively. Comparisons of baseline and “Sen”
simulations results show that the modeled grid-scale O₃ stomatal uptake and total Nr deposition are sensitive to the choice of
WACCM’s fire emission input (Fig. S22). This set of sensitivity analysis not only supports the findings about fire emission

impacts on deposition from offline air quality modeling studies (e.g., Koplitz et al., 2021), but also stresses the importance of accounting for aerosol radiative effects in assessing ecosystem impacts of pollutants from biomass burning and other sources, which will be investigated further on multiple spatiotemporal scales in an Hemispheric Transport of Air Pollution phase 3 multimodel experiment (Whaley et al., 2024, <https://doi.org/10.5194/gmd-2024-126>, in review).

Previous work has focused strongly on the impacts of long-range transport of pollution from Asia and the stratosphere, as well as regional pollution transport, on the western US O₃ trends (e.g., Cooper et al., 2012; Huang et al., 2013; Lin et al., 2017; Miyazaki et al., 2022). This case study demonstrates that extra-regional pollution can also compromise the efforts of improving air quality via controlling local and regional emissions over the eastern US. Possibly linked to climate change, such highly polluted events occurred more frequently during the 2023 warm season. For example, driven by hot and dry conditions, the Canadian 2023 wildfire season had the largest area burned in history (<https://cwfis.cfs.nrcan.gc.ca/ha/nfdb>, last access: 23 July). Due to Canadian wildfire impacts, there were at least two other known extreme air pollution events over the eastern US in June 2023 and more in the other months of the season (Fig. S24). Such events exerted controls on surface-atmosphere exchange processes and perturbing the long-term changes in O₃, Nr and other chemical compounds. More accurate and consistently-configured chemical BC models or reanalysis products, preferably at higher resolutions with a more complete list of prognostic and diagnostic variables, are essential for further regional-scale modeling investigations on such events and their contributions to trends/variability. Addition of stratospheric tracers and accurate, time-varying upper chemical boundary conditions to regional models, assisted with O₃ profile measurements from commercial aircraft, sondes, and Lidar networks, are expected to be also helpful for diagnosing and/or reducing errors in the simulations of some of such events.

4 Summary and suggested future directions

Based on WRF-Chem model simulations and multiplatform observations, this paper discussed Nr and O₃ concentrations and fluxes during 2018–2023 in the northeastern and mid-Atlantic US, most of which fell into NO_x-limited and transitional chemical regimes. Effective local emission controls resulted in evident decreases in NO₂ and surface O₃ concentrations, with the reduced human activities during the COVID lockdowns also contributing to their low values and the overall stronger surface O₃-NO₂ column correlations in 2020. Current polar-orbiting satellites take snapshots of NO₂ columns only at a particular time of day, such as in the early afternoon when surface NO₂ experienced their daily lows. With this sparse temporal sampling, TROPOMI did not miss the general NO₂ interannual and seasonal variability and filled in the extremely large horizontal gaps between surface AQS observations most of which are in/near urban regions and positively biased. The WRF-Chem simulation described here has been extended into 2024, running on a routine basis, to support refined analyses concerning the subdaily variability of NO₂ and other variables along with data from geostationary satellite missions such as the TEMPO.

630

The declines in NO_y emissions and concentrations were roughly consistent with the temporal changes in NO_y deposition, which were balanced out by the overall rising agricultural and total NH_x emissions and deposition. The changes in NO_y and NH_x deposition together shaped the interannual variability in Nr deposition in contrast to the clearer downward trends in O₃ vegetation uptake that reduced plants' water use efficiency and caused biomass/crop yield losses by a few percent. Certain hotspots of Nr deposition in North Carolina may have continued to exceed the CL thresholds for herbaceous plants and trees in literature, while the productivity of northern forests may have remained to be nitrogen-limited. Referring to the conservative lichen CL thresholds in literature, widespread lichen CL exceedances likely occurred persistently. Integrating nitrogen dynamics into LSMs could help improve their performance on land surface states as well as carbon, water, and energy fluxes, and further, the representations of Nr and O₃ deposition processes and their interactions in coupled modeling systems. Standard versions of Noah-MP, including what was used in this work, represent nitrogen stress by applying constant foliage nitrogen factors (<1) in maximum carboxylation rate calculations (Niu et al., 2011). Following the JULES and Community Land Model, Cai et al. (2016) started to add nitrogen dynamics to Noah-MP. Running offline, their updated model yielded more accurate net primary productivity and evapotranspiration, and that may also be embedded into Earth system models in future, with the magnitudes and spatiotemporal variability of its Nr inputs (e.g., from deposition and fertilizer applications) being improved with the aid of atmospheric chemistry model routines or/and observations. Other areas for improvements include assimilating additional Earth observations (e.g., rootzone SM and terrestrial water storage); developing and applying high-quality, spatially and temporally varying CO₂ forcings for Noah-MP; and tuning parameters that represent O₃ vegetation impacts for various types of plants at different growth stages.

With updated model parameterizations and anth emissions, the used WRF-Chem system performed stably and remarkably better on eastern US surface O₃ than many of those in literature. This paper highlighted that, temporal variability of Nr and O₃ concentrations and fluxes on subregional-to-local scales were partially driven by hydrological variability that can be influenced by precipitation and controllable human activities such as irrigation. Like deposition processes, biogenic soil Nr and VOC emissions that are highly sensitive to various climatic factors and plants' physiological conditions, as well as extra-regional sources (e.g., dense wildfire plumes from the western US and Canada, and O₃-rich stratospheric air), have been playing increasingly important roles in controlling pollutants' budgets in this area as local emissions went down. These outcomes based on this particular WRF-Chem system have implications for updating other modeling systems.

It is worth noting that, urban emissions and air pollutants can be transported to and deposited into rural and remote regions, which may better be modeled at finer resolutions (e.g., urban scale at 1–4 km or street-to-building scales) with the urban landscapes and human influences on urban vegetation and soil properties being more carefully handled. Finer model resolutions may also allow more processes, such as convection, to be explicitly resolved, potentially leading to more accurate precipitation and deposition results. Successful finer-resolution simulations would require accurate inputs and observational constraints at similar resolutions. To better inform the designs of mitigation and adaptation strategies, it is highly

665 recommended to continue evaluating and improving the parameterizations and inputs relevant to various sources and processes in seamlessly coupled multiscale Earth system models using laboratory and field experiments in combination with satellite DA. Further improved Earth system model results are expected to in turn benefit remote sensing communities, for example, via serving as the retrieval *a priori* profiles for different types of environments.

Code and data availability

670 NASA-Unified Weather Research and Forecasting model (<https://nuwrf.gsfc.nasa.gov/software>, last access: 6 February 2024) output of O₃ and other key variables will be shared via Zenodo with the final version of this manuscript. Remote sensing and in situ data sets can be downloaded from: <https://doi.org/10.5067/4DQ54OUIJ9DL> (O’Neill et al., 2021), <https://doi.org/10.5067/GPM/IMERGDF/DAY/07> (Huffman et al., 2023); <https://doi.org/10.5067/MHH8R0UZ5BMJ> (Bowman, 2022a); <https://doi.org/10.5067/JL1HT3NGEAW3> (Bowman, 2022b); <https://doi.org/10.5067/6HTQB4F81S08> (Bowman, 2022c); <https://www-air.larc.nasa.gov/cgi-bin/ArcView/listos> (Janz, 2020); <https://doi.org/10.5065/4F4P-E398> (NCEP, 2004); and https://aqs.epa.gov/aqsweb/airdata/download_files.html (US EPA, 2024, last access: 1 October 2024). Gridded TROPOMI data have been submitted by Isabelle De Smedt to TOAR-II Tropospheric Ozone Precursors Focus Group repository.

Author contributions

680 Overall study design and paper writing: MH leading, all participated in reviewing and editing
Design, execution, or discussions of model simulations: MH, GRC, SVK, ABG
Satellite data production, validation, delivery, and analysis: KWB, IDS, AC, MHC, MH
Field campaign deployments and data analysis: AC, MHC, SJJ, RMS, AMT, NMF, RJS, JDB, ATJ, MH

Competing interests

685 The authors declare that they have no competing interests.

Acknowledgements

NASA SMAP, SMAPVEX22 and LDAS sponsored part of the work. A contribution was made to this work at the Jet Propulsion Laboratory, California Institute of Technology, under a contract with NASA. We acknowledge the excellent leadership of TOAR-II Tropospheric Ozone Precursors and Deposition Focus Group leads. We thank Antonin Soulie and
690 team for helping with the CAMS global anth emissions, and Kyle DeLong for participating in collecting SM data in Harvard Forest during SMAPVEX22 that are used in this study. Color palettes in Crameri et al. (2020) are used in this paper.

References

- Aman, M. S., Jafari, M., Reihan, M. K., Motesharezadeh, B., and Zare, S.: Assessing the Effect of Industrial Wastewater on Soil Properties and Physiological and Nutritional Responses of Robinia Pseudoacacia, Cercis Siliquastrum and Caesalpinia
695 Gilliesii Seedlings, *J. Environ. Manag.*, <https://doi.org/10.1016/j.jenvman.2018.03.087>, 217, 718–726, 2018.
- Bowman, K. W.: TROPES CrIS-JPSS1 L2 Ozone for Forward Stream Summary Product, Version 1, Greenbelt, MD, USA, Goddard Earth Sciences Data and Information Services Center (GES DISC) [data set], Greenbelt, Maryland, USA, <https://doi.org/10.5067/MHH8R0UZ5BMJ>, 2022a.
700
- Bowman, K. W.: TROPES CrIS-JPSS1 L2 Carbon Monoxide for Forward Stream Summary Product, Version 1, Greenbelt, MD, USA, Goddard Earth Sciences Data and Information Services Center (GES DISC) [data set], Greenbelt, Maryland, USA, <https://doi.org/10.5067/JL1HT3NGEAW3>, 2022b.
- 705 Bowman, K. W.: TROPES CrIS-JPSS1 L2 Peroxyacetyl Nitrate for Forward Stream Summary Product, Version 1, Greenbelt, MD, USA, Goddard Earth Sciences Data and Information Services Center (GES DISC) [data set], Greenbelt, Maryland, USA, <https://doi.org/10.5067/6HTQB4F81S08>, 2022c.
- Cai, X., Yang, Z.-L., Fisher, J. B., Zhang, X., Barlage, M., and Chen, F.: Integration of nitrogen dynamics into the Noah-MP
710 land surface model v1.1 for climate and environmental predictions, *Geosci. Model Dev.*, 9, 1–15, <https://doi.org/10.5194/gmd-9-1-2016>, 2016.
- Carlton, A. G., Pinder, R. W., Bhave, P. V., and Pouliot, G. A.: To What Extent Can Biogenic SOA be Controlled? *Environ. Sci. Technol.*, 44, 3376–3380, <https://doi.org/10.1021/es903506b>, 2010.

715

Chai, T., Carmichael, G. R., Tang, Y., Sandu, A., Hardesty, M., Pilewskie, P., Whitlow, S., Browell, E. V., Avery, M. A., Nédélec, P., Merrill, J. T., Thompson, A. M., and Williams, E.: Four-dimensional data assimilation experiments with International Consortium for Atmospheric Research on Transport and Transformation ozone measurements, *J. Geophys. Res.*, 112, D12S15, <https://doi.org/10.1029/2006JD007763>, 2007.

720

Chai, T., Kim, H.-C., Lee, P., Tong, D., Pan, L., Tang, Y., Huang, J., McQueen, J., Tsidulko, M., and Stajner, I.: Evaluation of the United States National Air Quality Forecast Capability experimental real-time predictions in 2010 using Air Quality System ozone and NO₂ measurements, *Geosci. Model Dev.*, 6, 1831–1850, <https://doi.org/10.5194/gmd-6-1831-2013>, 2013.

725 Clifton, O. E., Lombardozzi, D. L., Fiore, A. M., Paulot, F., and Horowitz, L. W.: Stomatal conductance influences interannual variability and long-term changes in regional cumulative plant uptake of ozone, *Environ. Res. Lett.*, 15, 114059, <https://doi.org/10.1088/1748-9326/abc3f1>, 2020.

730 Colarco, P. R., Schoeberl, M. R., Doddridge, B. G., Marufu, L. T., Torres, O., and Welton, E. J.: Transport of smoke from Canadian forest fires to the surface near Washington, D.C.: Injection height, entrainment, and optical properties, *J. Geophys. Res.*, 109, D06203, <https://doi.org/10.1029/2003JD004248>, 2004.

735 Cook, B. I., Mankin, J. S., Marvel, K., Williams, A. P., Smerdon, J. E., and Anchukaitis, K. J.: Twenty-first century drought projections in the CMIP6 forcing scenarios, *Earth's Future*, 8, e2019EF001461, <https://doi.org/10.1029/2019EF001461>, 2020.

740 Cooper, O. R., Stohl, A., Eckhardt, S., Parrish, D. D., Oltmans, S. J., Johnson, B. J., Nédélec, P., Schmidlin, F. J., Newchurch, M. J., Kondo, Y., and Kita, K.: A springtime comparison of tropospheric ozone and transport pathways on the east and west coasts of the United States, *J. Geophys. Res.*, 110, D05S90, <https://doi.org/10.1029/2004JD005183>, 2005.

740

Cooper, O. R., Gao, R.-S., Tarasick, D., Leblanc, T., and Sweeney, C.: Long-term ozone trends at rural ozone monitoring sites across the United States, 1990–2010, *J. Geophys. Res.*, 117, D22307, <https://doi.org/10.1029/2012JD018261>, 2012.

745 Crameri, F., Shephard, G. E., and Heron, P. J.: The misuse of colour in science communication, *Nat. Commun.*, 11, 5444, <https://doi.org/10.1038/s41467-020-19160-7>, 2020.

Darmenov, A. and da Silva, A.: The Quick Fire Emissions Dataset (QFED): Documentation of versions 2.1, 2.2 and 2.4, NASA Technical Report Series, Global Modeling and Data Assimilation, NASA TM-2015-104606/Volume 38, available at: <http://gmao.gsfc.nasa.gov/pubs/docs/Darmenov796.pdf> (last access: 12 January 2023), 2015.

750

De Smedt, I., Pinardi, G., Vigouroux, C., Compernelle, S., Bais, A., Benavent, N., Boersma, F., Chan, K.-L., Donner, S., Eichmann, K.-U., Hedelt, P., Hendrick, F., Irie, H., Kumar, V., Lambert, J.-C., Langerock, B., Lerot, C., Liu, C., Loyola, D., Pitters, A., Richter, A., Rivera Cárdenas, C., Romahn, F., Ryan, R. G., Sinha, V., Theys, N., Vlietinck, J., Wagner, T., Wang, T., Yu, H., and Van Roozendael, M.: Comparative assessment of TROPOMI and OMI formaldehyde observations and validation against MAX-DOAS network column measurements, *Atmos. Chem. Phys.*, 21, 12561–12593, <https://doi.org/10.5194/acp-21-12561-2021>, 2021.

755

Dentener, F., Drevet, J., Lamarque, J. F., Bey, I., Eickhout, B., Fiore, A. M., Hauglustaine, D., Horowitz, L. W., Krol, M., Kulshrestha, U. C., Lawrence, M., Galy-Lacaux, C., Rast, S., Shindell, D., Stevenson, D., Van Noije, T., Atherton, C., Bell, N., Bergman, D., Butler, T., Cofala, J., Collins, B., Doherty, R., Ellingsen, K., Galloway, J., Gauss, M., Montanaro, V., Müller, J. F., Pitari, G., Rodriguez, J., Sanderson, M., Solmon, F., Strahan, S., Schultz, M., Sudo, K., Szopa, S., and Wild, O.: Nitrogen and sulfur deposition on regional and global scales: A multimodel evaluation, *Global Biogeochem. Cy.*, 20, B4003, <https://doi.org/10.1029/2005GB002672>, 2006.

760

Delaria, E. R. and Cohen, R. C.: Measurements of Atmosphere–Biosphere Exchange of Oxidized Nitrogen and Implications for the Chemistry of Atmospheric NO_x, *Acc. Chem. Res.*, 56, 1720–1730, <https://doi.org/10.1021/acs.accounts.3c00090>, 2023.

765

Dix, B., Francoeur, C., Li, M., Serrano-Calvo, R., Levelt, P. F., Veeffkind, J. P., McDonald, B. C., and de Gouw, J.: Quantifying NO_x Emissions from U.S. Oil and Gas Production Regions Using TROPOMI NO₂, *ACS Earth and Space Chem.*, 6, 403–414, <https://doi.org/10.1021/acsearthspacechem.1c00387>, 2022.

770

Doumbia, T., Granier, C., Elguindi, N., Bouarar, I., Darras, S., Brasseur, G., Gaubert, B., Liu, Y., Shi, X., Stavrakou, T., Tilmes, S., Lacey, F., Deroubaix, A., and Wang, T.: Changes in global air pollutant emissions during the COVID-19 pandemic: a dataset for atmospheric modeling, *Earth Syst. Sci. Data*, 13, 4191–4206, <https://doi.org/10.5194/essd-13-4191-2021>, 2021.

775

Draper, C. and Reichle, R.: The impact of near-surface soil moisture assimilation at subseasonal, seasonal, and inter-annual timescales, *Hydrol. Earth Syst. Sci.*, 19, 4831–4844, <https://doi.org/10.5194/hess-19-4831-2015>, 2015.

780

- Du, E., Terrer, C., Pellegrini, A.F.A., Ahlström, A., van Lissa, C. J., Zhao, X., Xia, N., Wu, X., and Jackson, R. B.: Global patterns of terrestrial nitrogen and phosphorus limitation, *Nat. Geosci.*, 13, 221–226, <https://doi.org/10.1038/s41561-019-0530-4>, 2020.
- 785 Duncan, B. N., Yoshida, Y., Olson, J. R., Sillman, S., Martin, R. V., Lamsal, L., Hu, Y., Pickering, K. E., Retscher, C., Allen, D. J., and Crawford, J. H.: Application of OMI observations to a space-based indicator of NO_x and VOC controls on surface ozone formation, *Atmos. Environ.*, 44, 2213–2223, <https://doi.org/10.1016/j.atmosenv.2010.03.010>, 2010.
- Dunlea, E. J., Herndon, S. C., Nelson, D. D., Volkamer, R. M., San Martini, F., Sheehy, P. M., Zahniser, M. S., Shorter, J.
790 H., Wormhoudt, J. C., Lamb, B. K., Allwine, E. J., Gaffney, J. S., Marley, N. A., Grutter, M., Marquez, C., Blanco, S., Cardenas, B., Retama, A., Ramos Villegas, C. R., Kolb, C. E., Molina, L. T., and Molina, M. J.: Evaluation of nitrogen dioxide chemiluminescence monitors in a polluted urban environment, *Atmos. Chem. Phys.*, 7, 2691–2704, <https://doi.org/10.5194/acp-7-2691-2007>, 2007.
- 795 Elguindi, N., Granier, C., Stavrou, T., Darras, S., Bauwens, M., Cao, H., Chen, C., Denier van der Gon, H. A. C., Dubovik, O., Fu, T. M., Henze, D. K., Jiang, Z., Keita, S., Kuenen, J. J. P., Kurokawa, J., Liousse, C., Miyazaki, K., Müller, J. F., Qu, Z., Solomon, F., and Zheng, B.: Intercomparison of Magnitudes and Trends in Anthropogenic Surface Emissions From Bottom-Up Inventories, Top-Down Estimates, and Emission Scenarios, *Earths Future*, 8, e2020EF001520, <https://doi.org/10.1029/2020EF001520>, 2020.
- 800 Emberson, L.: Effects of ozone on agriculture, forests and grasslands, *Phil. Trans. R. Soc. A.*, 378, 20190327, <https://doi.org/10.1098/rsta.2019.0327>, 2020.
- Erismann, J. W., Van Pul, A., and Wyers, P.: Parameterization of surface resistance for the quantification of atmospheric
805 deposition of acidifying pollutants and ozone, *Atmos. Environ.*, 28, 2595–2607, [https://doi.org/10.1016/1352-2310\(94\)90433-2](https://doi.org/10.1016/1352-2310(94)90433-2), 1994.
- Eskes, H. J. and Boersma, K. F.: Averaging kernels for DOAS total-column satellite retrievals, *Atmos. Chem. Phys.*, 3, 1285–1291, <https://doi.org/10.5194/acp-3-1285-2003>, 2003.
- 810 Felzer, B. S., Cronin, T. W., Melillo, J. M., Kicklighter, D. W., and Schlosser, C. A.: Importance of carbon-nitrogen interactions and ozone on ecosystem hydrology during the 21st century, *J. Geophys. Res.*, 114, G01020, <https://doi.org/10.1029/2008JG000826>, 2009.

815 Fiore, A. M., Dentener, F. J., Wild, O., Cuvelier, C., Schultz, M. G., Hess, P., Textor, C., Schulz, M., Doherty, R. M., Horowitz, L. W., MacKenzie, I. A., Sanderson, M. G., Shindell, D. T., Stevenson, D. S., Szopa, S., van Dingenen, R., Zeng, G., Atherton, C., Bergmann, D., Bey, I., Carmichael, G., Collins, W. J., Duncan, B. N., Faluvegi, G., Folberth, G., Gauss, M., Gong, S., Hauglustaine, D., Holloway, T., Isaksen, I. S. A., Jacob, D. J., Jonson, J. E., Kaminski, J. W., Keating, T. J., Lupu, A., Marnmer, E., Montanaro, V., Park, R. J., Pitari, G., Pringle, K. J., Pyle, J. A., Schroeder, S., Vivanco, M. G., Wind,
820 P., Wojcik, G., Wu, S., and Zuber, A.: Multimodel estimates of intercontinental source-receptor relationships for ozone pollution, *J. Geophys. Res.*, 114, D04301, <https://doi.org/10.1029/2008JD010816>, 2009.

Fu, J. S., Carmichael, G. R., Dentener, F., Aas, W., Andersson, C., Barrie, L. A., Cole, A., Galy-Lacaux, C., Geddes, J., Itahashi, S., Kanakidou, M., Labrador, L., Paulot, F., Schwede, D., Tan, J., and Vet, R.: Improving Estimates of Sulfur,
825 Nitrogen, and Ozone Total Deposition through Multi-Model and Measurement-Model Fusion Approaches, *Environ. Sci. Technol.*, 56, 2134–2142, <https://doi.org/10.1021/acs.est.1c05929>, 2022.

Galloway, J. N., Aber, J. D., Erisman, J. W., Seitzinger, S. P., Howarth, R. W., Cowling, E. B., and Cosby, B. J.: The nitrogen cascade, *Bioscience*, 53, 341–356, [https://doi.org/10.1641/0006-3568\(2003\)053\[0341:TNC\]2.0.CO;2](https://doi.org/10.1641/0006-3568(2003)053[0341:TNC]2.0.CO;2), 2003.

830

Galloway, J. N., Dentener, F. J., Capone, D. G., Boyer, E. W., Howarth, R. W., Seitzinger, S. P., Asner, G. P., Cleveland, C. C., Green, P. A., Holland, E. A., Karl, D. M., Michaels, A. F., Porter, J. H., Townsend, A. R., and Vorosmarty, C. J.: Nitrogen cycles: past, present, and future, *Biogeochemistry*, 70, 153–226, <https://doi.org/10.1007/s10533-004-0370-0>, 2004.

835 Gaudel, A., Cooper, O. R., Ancellet, G., Barret, B., Boynard, A., Burrows, J. P., Clerbaux, C., Coheur, P. F., Cuesta, J., Cuevas, E., Doniki, S., Dufour, G., Ebojje, F., Foret, G., Garcia, O., Granados-Munoz, M. J., Hannigan, J. W., Hase, F., Hassler, B., Huang, G., Hurtmans, D., Jaffe, D., Jones, N., Kalabokas, P., Kerridge, B., Kulawik, S., Latter, B., Leblanc, T., Le Flochmoen, E., Lin, W., Liu, J., Liu, X., Mahieu, E., McClure-Begley, A., Neu, J. L., Osman, M., Palm, M., Petetin, H., Petropavlovskikh, I., Querel, R., Rapp, N., Rozanov, A., Schultz, M. G., Schwab, J., Siddans, R., Smale, D., Steinbacher,
840 M., Tanimoto, H., Tarasick, D. W., Thouret, V., Thompson, A. M., Trickl, T., Weatherhead, E., Wespes, C., Worden, H. M., Vigouroux, C., Xu, X., Zeng, G., and Ziemke, J.: Tropospheric Ozone Assessment Report: Present-day distribution and trends of tropospheric ozone relevant to climate and global atmospheric chemistry model evaluation, *Elementa-Sci. Anthropol.*, 6, 39, <https://doi.org/10.1525/elementa.291>, 2018.

845 Geddes, J. A. and Martin, R. V.: Global deposition of total reactive nitrogen oxides from 1996 to 2014 constrained with satellite observations of NO₂ columns, *Atmos. Chem. Phys.*, 17, 10071–10091, <https://doi.org/10.5194/acp-17-10071-2017>, 2017.

Geiser, L. H., Nelson, P. R., Jovan, S. E., Root, H. T., and Clark, C. M.: Assessing Ecological Risks from Atmospheric
850 Deposition of Nitrogen and Sulfur to US Forests Using Epiphytic Macrolichens, *Diversity*, 2019; 11, 87,
<https://doi.org/10.3390/d11060087>, 2019.

Georgoulas, A. K., Boersma, K. F., van Vliet, J., Zhang, X., van der A, R., Zanis, P., and de Laat, J.: Detection of NO₂
pollution plumes from individual ships with the TROPOMI/S5P satellite sensor, *Environ. Res. Lett.*, 15, 124037,
855 <https://doi.org/10.1088/1748-9326/abc445>, 2020.

Goldberg, D. L., Anenberg, S. C., Kerr, G. H., Moheg, A., Lu, Z., and Streets, D. G.: TROPOMI NO₂ in the United States:
A detailed look at the annual averages, weekly cycles, effects of temperature, and correlation with surface NO₂
concentrations, *Earth's Future*, 9, e2020EF001665, <https://doi.org/10.1029/2020EF001665>, 2021.

860

Granier, C., S. Darras, H. Denier van der Gon, J. Doubalova, N. Elguindi, B. Galle, M. Gauss, M. Guevara, J.-P. Jalkanen, J.
Kuenen, C. Lioussé, B. Quack, D. Simpson, K. Sindelarova, The Copernicus Atmosphere Monitoring Service global and
regional emissions, Copernicus Atmosphere Monitoring Service report, <https://doi.org/10.24380/d0bn-kx16>, 2019.

865 Grell, G., Freitas, S. R., Stuefer, M., and Fast, J.: Inclusion of biomass burning in WRF-Chem: impact of wildfires on
weather forecasts, *Atmos. Chem. Phys.*, 11, 5289–5303, <https://doi.org/10.5194/acp-11-5289-2011>, 2011.

Griffin, D., McLinden, C. A., Dammers, E., Adams, C., Stockwell, C. E., Warneke, C., Bourgeois, I., Peischl, J., Ryerson, T.
B., Zarzana, K. J., Rowe, J. P., Volkamer, R., Knute, C., Kille, N., Koenig, T. K., Lee, C. F., Rollins, D., Rickly, P. S., Chen,
870 J., Fehr, L., Bourassa, A., Degenstein, D., Hayden, K., Mihele, C., Wren, S. N., Liggio, J., Akingunola, A., and Makar, P.:
Biomass burning nitrogen dioxide emissions derived from space with TROPOMI: methodology and validation, *Atmos.
Meas. Tech.*, 14, 7929–7957, <https://doi.org/10.5194/amt-14-7929-2021>, 2021.

Harmens, H., Hayes, F., Sharps, K., Radbourne, A., and Mills, G.: Can Reduced Irrigation Mitigate Ozone Impacts on an
875 Ozone-Sensitive African Wheat Variety? *Plants*, 8, 220, <https://doi.org/10.3390/plants8070220>, 2019.

Holt, J., Selin, N. E., and Solomon, S.: Changes in Inorganic Fine Particulate Matter Sensitivities to Precursors Due to
Large-Scale US Emissions Reductions, *Environ. Sci. Technol.*, 49, 4834–4841, <https://doi.org/10.1021/acs.est.5b00008>,
2015.

880

Horn, K. J., Thomas, R. Q., Clark, C. M., Pardo, L. H., Fenn, M. E., Lawrence, G. B., Perakis, S. S., Smithwick, E. A. H.,
Baldwin, D., Braun, S., Nordin, A., Perry, C. H., Phelan, J. N., Schaberg, P. G., St. Clair, S. B., Warby, R., and Watmough,

S.: Growth and survival relationships of 71 tree species with nitrogen and sulfur deposition across the conterminous U.S., *PLoS ONE*, 13, e0205296, <https://doi.org/10.1371/journal.pone.0205296>, 2018.

885

Huang, M., Bowman, K. W., Carmichael, G. R., Pierce, R. B., Worden, H. M., Luo, M., Cooper, O. R., Pollack, I. B., Ryerson, T. B., and Brown, S. S.: Impact of Southern California anthropogenic emissions on ozone pollution in the mountain states: Model analysis and observational evidence from space, *J. Geophys. Res. Atmos.*, 118, 12,784–12,803, <https://doi.org/10.1002/2013JD020205>, 2013.

890

Huang, M., Carmichael, G. R., Pierce, R. B., Jo, D. S., Park, R. J., Flemming, J., Emmons, L. K., Bowman, K. W., Henze, D. K., Davila, Y., Sudo, K., Jonson, J. E., Tronstad Lund, M., Janssens-Maenhout, G., Dentener, F. J., Keating, T. J., Oetjen, H., and Payne, V. H.: Impact of intercontinental pollution transport on North American ozone air pollution: an HTAP phase 2 multi-model study, *Atmos. Chem. Phys.*, 17, 5721–5750, <https://doi.org/10.5194/acp-17-5721-2017>, 2017a.

895

Huang, M., Carmichael, G. R., Crawford, J. H., Wisthaler, A., Zhan, X., Hain, C. R., Lee, P., and Guenther, A. B.: Biogenic isoprene emissions driven by regional weather predictions using different initialization methods: case studies during the SEAC⁴RS and DISCOVER-AQ airborne campaigns, *Geosci. Model Dev.*, 10, 3085–3104, <https://doi.org/10.5194/gmd-10-3085-2017>, 2017b.

900

Huang, M., Crawford, J. H., Carmichael, G. R., Santanello, J. A., Kumar, S. V., Stauffer, R. M., Thompson, A. M., Weinheimer, A.J., and Park, J. D.: Impact of aerosols from urban and shipping emission sources on terrestrial carbon uptake and evapotranspiration: A case study in east Asia, *J. Geophys. Res. Atmos.*, 125, e2019JD030818, <https://doi.org/10.1029/2019JD030818>, 2020.

905

Huang, M., Crawford, J. H., DiGangi, J. P., Carmichael, G. R., Bowman, K. W., Kumar, S. V., and Zhan, X.: Satellite soil moisture data assimilation impacts on modeling weather variables and ozone in the southeastern US – Part 1: An overview, *Atmos. Chem. Phys.*, 21, 11013–11040, <https://doi.org/10.5194/acp-21-11013-2021>, 2021.

910 Huang, M., Crawford, J. H., Carmichael, G. R., Bowman, K. W., Kumar, S. V., and Sweeney, C.: Satellite soil moisture data assimilation impacts on modeling weather variables and ozone in the southeastern US – Part 2: Sensitivity to dry-deposition parameterizations, *Atmos. Chem. Phys.*, 22, 7461–7487, <https://doi.org/10.5194/acp-22-7461-2022>, 2022.

Hudman, R. C., Moore, N. E., Mebust, A. K., Martin, R. V., Russell, A. R., Valin, L. C., and Cohen, R. C.: Steps towards a
915 mechanistic model of global soil nitric oxide emissions: implementation and space based-constraints, *Atmos. Chem. Phys.*, 12, 7779–7795, <https://doi.org/10.5194/acp-12-7779-2012>, 2012.

Huffman, G. J., Stocker, E. F., Bolvin, D. T., Nelkin, E. J., and Tan, J.: GPM IMERG Final Precipitation L3 1 day 0.1 degree
×0.1 degree, Version 7, Goddard Earth Sciences Data and Information Services Center (GES DISC) [data set], Greenbelt,
920 Maryland, USA, <https://doi.org/10.5067/GPM/IMERGDF/DAY/07>, 2023.

Janz, S.: Long Island Sound Tropospheric Ozone Study GCAS and GeoTASO measurements of NO₂ and CH₂O, Version R1,
NASA Langley Research Center Airborne Science Data for Atmospheric Composition [data set], Hampton, Virginia, USA,
available at: <https://www-air.larc.nasa.gov/missions/listos/index.html> (last access: 6 February 2024), 2020.

925

Jia, Y., Yu, G., Gao, Y., He, N., Wang, Q., Jiao, C., and Zuo, Y.: Global inorganic nitrogen dry deposition inferred from
ground- and space-based measurements, *Sci. Rep.*, 6, 19810, <https://doi.org/10.1038/srep19810>, 2016.

Jiang, X., Guenther, A., Potosnak, M., Geron, C., Seco, R., Karl, T., Kim, S., Gu, L., and Pallardy, S.: Isoprene emission
930 response to drought and the impact on global atmospheric chemistry, *Atmos. Environ.*, 183, 69–83,
<https://doi.org/10.1016/j.atmosenv.2018.01.026>, 2018.

Jin, X., Fiore, A. M., Murray, L. T., Valin, L. C., Lamsal, L. N., Duncan, B., Boersma, K. F., De Smedt, I., Abad, G. G.,
Chance, K., and Tonnesen, G. S.: Evaluating a Space-Based Indicator of Surface Ozone-NO_x-VOC Sensitivity Over
935 Midlatitude Source Regions and Application to Decadal Trends, *J. Geophys. Res.-Atmos.*, 122, 10439–10461,
<https://doi.org/10.1002/2017JD026720>, 2017.

Judd, L. M., Al-Saadi, J. A., Szykman, J. J., Valin, L. C., Janz, S. J., Kowalewski, M. G., Eskes, H. J., Veefkind, J. P., Cede,
A., Mueller, M., Gebetsberger, M., Swap, R., Pierce, R. B., Nowlan, C. R., Abad, G. G., Nehrir, A., and Williams, D.:
940 Evaluating Sentinel-5P TROPOMI tropospheric NO₂ column densities with airborne and Pandora spectrometers near New
York City and Long Island Sound, *Atmos. Meas. Tech.*, 13, 6113–6140, <https://doi.org/10.5194/amt-13-6113-2020>, 2020.

Karion, A., Callahan, W., Stock, M., Prinzivalli, S., Verhulst, K. R., Kim, J., Salameh, P. K., Lopez-Coto, I., and Whetstone,
J.: Greenhouse gas observations from the Northeast Corridor tower network, *Earth Syst. Sci. Data*, 12, 699–717,
945 <https://doi.org/10.5194/essd-12-699-2020>, 2020.

Keller, C. A., Evans, M. J., Knowland, K. E., Hasenkopf, C. A., Modekurty, S., Lucchesi, R. A., Oda, T., Franca, B. B.,
Mandarino, F. C., Díaz Suárez, M. V., Ryan, R. G., Fakes, L. H., and Pawson, S.: Global impact of COVID-19 restrictions
on the surface concentrations of nitrogen dioxide and ozone, *Atmos. Chem. Phys.*, 21, 3555–3592,
950 <https://doi.org/10.5194/acp-21-3555-2021>, 2021.

- Kopplitz, S. N., Nolte, C. G., Sabo, R. D., Clark, C. M., Horn, K. J., Thomas, R. Q., and Newcomer-Johnson, T. A.: The contribution of wildland fire emissions to deposition in the US: Implications for tree growth and survival in the Northwest, *Environ. Res. Lett.*, 16, 024028, <https://doi.org/10.1088/1748-9326/abd26e>, 2021.
- 955
- Kopplitz, S., Simon, H., Henderson, B., Liljegren, J., Tonnesen, G., Whitehill, A., and Wells, B.: Changes in Ozone Chemical Sensitivity in the United States from 2007 to 2016, *ACS Environ. Au*, 2, 206–222, <https://doi.org/10.1021/acsenvironau.1c00029>, 2022.
- 960
- Kumar, S. V., Reichle, R. H., Koster, R. D., Crow, W. T., and Peters-Lidard, C. D.: Role of subsurface physics in the assimilation of surface soil moisture observations, *J. Hydrometeorol.*, 10, 1534–1547, <https://doi.org/10.1175/2009JHM1134.1>, 2009.
- Lapina, K., Henze, D. K., Milford, J. B., Huang, M., Lin, M., Fiore, A. M., Carmichael, G., Pfister, G. G., and Bowman, K.:
- 965
- Assessment of source contributions to seasonal vegetative exposure to ozone in the U.S., *J. Geophys. Res.-Atmos.*, 119, 324–340, <https://doi.org/10.1002/2013JD020905>, 2014.
- Li, C., Martin, R. V., Cohen, R. C., Bindle, L., Zhang, D., Chatterjee, D., Weng, H., and Lin, J.: Variable effects of spatial resolution on modeling of nitrogen oxides, *Atmos. Chem. Phys.*, 23, 3031–3049, <https://doi.org/10.5194/acp-23-3031-2023>,
- 970
- 2023.
- Li, J., Mahalov, A., and Hyde, P.: Simulating the impacts of chronic ozone exposure on plant conductance and photosynthesis, and on the regional hydroclimate using WRF/Chem, *Environ. Res. Lett.*, 11, 114017, <https://doi.org/10.1088/1748-9326/11/11/114017>, 2016.
- 975
- Li, Y., Schichtel, B. A., Walker, J. T., Schwede, D. B., Chen, X., Lehmann, C. M. B., Puchalski, M. A., Gay, D. A., and Collett Jr., J. L.: Increasing importance of deposition of reduced nitrogen in the United States, *Proc. Natl. Acad. Sci. USA*, 113, 5874–5879, <https://doi.org/10.1073/pnas.1525736113>, 2016.
- 980
- Lin, M., Horowitz, L. W., Payton, R., Fiore, A. M., and Tonnesen, G.: US surface ozone trends and extremes from 1980 to 2014: quantifying the roles of rising Asian emissions, domestic controls, wildfires, and climate, *Atmos. Chem. Phys.*, 17, 2943–2970, <https://doi.org/10.5194/acp-17-2943-2017>, 2017.

- 985 Liu, L., Zhang, X., Xu, W., Liu, X., Wei, J., Wang, Z., and Yang, Y.: Global estimates of dry ammonia deposition inferred from space-measurements, *Sci. Total Environ.*, 730, 139189, <https://doi.org/10.1016/j.scitotenv.2020.139189>, 2020a.
- Liu, L., Zhang, X., Xu, W., Liu, X., Lu, X., Wei, J., Li, Y., Yang, Y., Wang, Z., and Wong, A. Y. H.: Reviewing global estimates of surface reactive nitrogen concentration and deposition using satellite retrievals, *Atmos. Chem. Phys.*, 20, 8641–8658, <https://doi.org/10.5194/acp-20-8641-2020>, 2020b.
- 990 Liu, J., Clark, L. P., Bechle, M., Hajat, A., Kim, S.-Y., Robinson, A., Sheppard, Lianne, Szpiro, A. A., and Marshall, J. D.: Disparities in air pollution exposure in the United States by race-ethnicity and income, 1990–2010, *Environ. Health Perspect.*, 129, 127005, <https://doi.org/10.1289/EHP8584>, 2021.
- 995 Lombardozzi, D., Levis, S., Bonan, G., Hess, P. G., and Sparks, J. P.: The Influence of Chronic Ozone Exposure on Global Carbon and Water Cycles, *J. Climate*, 28, 292–305, <https://doi.org/10.1175/JCLI-D-14-00223.1>, 2015.
- Lorente, A., Boersma, K. F., Yu, H., Dörner, S., Hilboll, A., Richter, A., Liu, M., Lamsal, L. N., Barkley, M., De Smedt, I., Van Roozendaal, M., Wang, Y., Wagner, T., Beirle, S., Lin, J.-T., Krotkov, N., Stammes, P., Wang, P., Eskes, H. J., and Krol, M.: Structural uncertainty in air mass factor calculation for NO₂ and HCHO satellite retrievals, *Atmos. Meas. Tech.*, 10, 759–782, <https://doi.org/10.5194/amt-10-759-2017>, 2017.
- 1000 Massad, R.-S., Nemitz, E., and Sutton, M. A.: Review and parameterisation of bi-directional ammonia exchange between vegetation and the atmosphere, *Atmos. Chem. Phys.*, 10, 10359–10386, <https://doi.org/10.5194/acp-10-10359-2010>, 2010.
- 1005 Mills, G., Sharps, K., Simpson, D., Pleijel, H., Broberg, M., Uddling, J., Jaramillo, F., Davies, W. J., Dentener, F., van den Berg, M., Agrawal, M., Agrawal, S. B., Ainsworth, E. A., Buker, P., Emberson, L., Feng, Z., Harmens, H., Hayes, F., Kopbayashi, K., Paoletti, E., and Van Dingenen, R.: Ozone pollution will compromise efforts to increase global wheat production, *Global Change Biol.*, 24, 3560–3574, <https://doi.org/10.1111/gcb.14157>, 2018.
- 1010 Miyazaki, K., Neu, J. L., Osterman, G., and Bowman, K.: Changes in US background ozone associated with the 2011 turnaround in Chinese NO_x emissions, *Environ. Res. Commun.*, 4, 045003, <https://doi.org/10.1088/2515-7620/ac619b>, 2022.
- 1015 Monfreda, C., Ramankutty, N., and Foley, J. A.: Farming the planet: 2. Geographic distribution of crop areas, yields, physiological types, and net primary production in the year 2000, *Global Biogeochem. Cycles*, 22, GB1022, <https://doi.org/10.1029/2007GB002947>, 2008.

Monks, P. S., Ravishankara, A. R., von Schneidmesser, E., and Sommariva, R.: Opinion: Papers that shaped tropospheric chemistry, *Atmos. Chem. Phys.*, 21, 12909–12948, <https://doi.org/10.5194/acp-21-12909-2021>, 2021.

1020

NCEP: NCEP ADP Global Surface Observational Weather Data, October 1999 – continuing, updated daily, Research Data Archive at the National Center for Atmospheric Research, Computational and Information Systems Laboratory [data set], Boulder, Colorado, USA, <https://doi.org/10.5065/4F4P-E398>, 2004.

1025 Nguyen, T. B., Crounse, J. D., Teng, A. P., Clair, J. M. S., Paulot, F., Wolfe, G. M., and Wennberg, P. O.: Rapid deposition of oxidized biogenic compounds to a temperate forest, *Proc. Natl. Acad. Sci. USA*, 112, E392–E401, <https://doi.org/10.1073/pnas.1418702112>, 2015.

Niu, G. Y., Yang, Z. L., Mitchell, K. E., Chen, F., Ek, M. B., Barlage, M., Kumar, A., Manning, K., Niyogi, D., Rosero, E.,
1030 Tewari, M., and Xia, Y.: The community Noah land surface model with multiparameterization options (Noah-MP): 1. Model description and evaluation with local-scale measurements, *J. Geophys. Res.-Atmos.*, 116, D12109, <https://doi.org/10.1029/2010JD015139>, 2011.

O’Neill, P. E., Chan, S., Njoku, E. G., Jackson, T., Bindlish, R., Chaubell, J., and Colliander, A.: SMAP Enhanced L3
1035 Radiometer Global and Polar Grid Daily 9 km EASE-Grid Soil Moisture, Version 5, NASA National Snow and Ice Data Center Distributed Active Archive Center [data set], Boulder, Colorado, USA, <https://doi.org/10.5067/4DQ54OUIJ9DL>, 2021.

Oswald, R., Behrendt, T., Ermel, M., Wu, D., Su, H., Cheng, Y., Breuninger, C., Moravek, A., Mougín, E., Delon, C.,
1040 Loubet, B., Pommerening-Röser, A., Sörgel, M., Pöschl, U., Hoffmann, T., Andreae, M. O., Meixner, F. X., and Trebs, I.: HONO emissions from soil bacteria as a major source of atmospheric reactive nitrogen, *Science*, 341, 1233–1235, <https://doi.org/10.1126/science.1242266>, 2013.

Ott, L. E., Duncan, B. N., Thompson, A. M., Diskin, G., Fasnacht, Z., Langford, A. O., Lin, M., Molod, A. M., Nielsen, J.
1045 E., Pusede, S. E., Wargan, K., Weinheimer, A. J., and Yoshida, Y.: Frequency and impact of summertime stratospheric intrusions over Maryland during DISCOVER-AQ (2011): New evidence from NASA's GEOS-5 simulations, *J. Geophys. Res.-Atmos.*, 121, 3687–3706, <https://doi.org/10.1002/2015JD024052>, 2016.

Pardo, L. H., Fenn, M.E., Goodale, C. L., Geiser, L. H., Driscoll, C. T., Allen, E. B., Baron, J. S., Bobbink, R., Bowman, W.
1050 D., Clark, C. M., Emmett, B., Gilliam, F. S., Greaver, T. L., Hall, S. J., Lilleskov, E. A., Liu, L., Lynch, J. A., Nadelhoffer, K. J., Perakis, S. S., Robin-Abbott, M. J., Stoddard, J. L., Weathers, K. C., and Dennis, R. L.: Effects of nitrogen deposition

and empirical nitrogen critical loads for ecoregions of the United States, *Ecol. Appl.*, 21, 3049–3082, <https://doi.org/10.1007/s11270014-2109-4>, 2011.

1055 Pleim, J. E., Ran, L., Appel, W., Shephard, M. W., and Cady-Pereira, K.: New bidirectional ammonia flux model in an air quality model coupled with an agricultural model, *J. Adv. Model. Earth Syst.*, 11, 2934–2957, <https://doi.org/10.1029/2019MS0017282934>, 2019.

Putero, D., Cristofanelli, P., Chang, K.-L., Dufour, G., Beachley, G., Couret, C., Effertz, P., Jaffe, D. A., Kubistin, D.,
1060 Lynch, J., Petropavlovskikh, I., Puchalski, M., Sharac, T., Sive, B. C., Steinbacher, M., Torres, C., and Cooper, O. R.: Fingerprints of the COVID-19 economic downturn and recovery on ozone anomalies at high-elevation sites in North America and western Europe, *Atmos. Chem. Phys.*, 23, 15693–15709, <https://doi.org/10.5194/acp-23-15693-2023>, 2023.

Rasool, Q. Z., Bash, J. O., and Cohan, D. S.: Mechanistic representation of soil nitrogen emissions in the Community
1065 Multiscale Air Quality (CMAQ) model v5.1, *Geosci. Model Dev.*, 12, 849–878, <https://doi.org/10.5194/gmd-12-849-2019>, 2019.

Rogers, H. M., Ditto, J. C., and Gentner, D. R.: Evidence for impacts on surface-level air quality in the northeastern US from
long-distance transport of smoke from North American fires during the Long Island Sound Tropospheric Ozone Study
1070 (LISTOS) 2018, *Atmos. Chem. Phys.*, 20, 671–682, <https://doi.org/10.5194/acp-20-671-2020>, 2020.

Rubin, H. J., Fu, J. S., Dentener, F., Li, R., Huang, K., and Fu, H.: Global nitrogen and sulfur deposition mapping using a
measurement–model fusion approach, *Atmos. Chem. Phys.*, 23, 7091–7102, <https://doi.org/10.5194/acp-23-7091-2023>,
2023.

1075 Ryu, Y.-H. and Min, S.-K.: Improving wet and dry deposition of aerosols in WRF-Chem: Updates to below-cloud scavenging and coarse-particle dry deposition, *J. Adv. Model. Earth Syst.*, 14, e2021MS002792, <https://doi.org/10.1029/2021MS002792>, 2022.

1080 Paulot, F., Jacob, D. J., and Henze, D. K.: Sources and Processes Contributing to Nitrogen Deposition: An Adjoint Model Analysis Applied to Biodiversity Hotspots Worldwide, *Environ. Sci. Technol.*, 47, 3226–3233, <https://doi.org/10.1021/es3027727>, 2013.

Paulot, F., Malyshev, S., Nguyen, T., Crouse, J. D., Shevliakova, E., and Horowitz, L. W.: Representing sub-grid scale
1085 variations in nitrogen deposition associated with land use in a global Earth system model: implications for present and future

- nitrogen deposition fluxes over North America, *Atmos. Chem. Phys.*, 18, 17963–17978, <https://doi.org/10.5194/acp-18-17963-2018>, 2018.
- 1090 Sadiq, M., Tai, A. P. K., Lombardozi, D., and Val Martin, M.: Effects of ozone–vegetation coupling on surface ozone air quality via biogeochemical and meteorological feedbacks, *Atmos. Chem. Phys.*, 17, 3055–3066, <https://doi.org/10.5194/acp-17-3055-2017>, 2017.
- Salmon, J. M., Friedl, M. A., Frohling, S., Wisser, D., and Douglas, E. M.: Global rain-fed, irrigated, and paddy croplands: A new high resolution map derived from remote sensing, crop inventories and climate data, *Int. J. Appl. Earth Obs.*, 38, 321–
1095 334, <https://doi.org/10.1016/j.jag.2015.01.014>, 2015.
- Schwede, D. B. and Lear, G. G.: A novel hybrid approach for estimating total deposition in the United States, *Atmos. Environ.*, 92, 207–220, <http://dx.doi.org/10.1016/j.atmosenv.2014.04.008>, 2014.
- 1100 Seinfeld, J. H. and Pandis, S. N.: *Atmospheric chemistry and physics: from air pollution to climate change*, Third edition, John Wiley & Sons, Inc., Hoboken, New Jersey, 2016.
- Seneviratne, S. I., Corti, T., Davin, E. L., Hirschi, M., Jaeger, E. B., Lehner, I., Orlowsky, B., and Teuling, A. J.: Investigating soil moisture-climate interactions in a changing climate: A review, *Earth-Sci. Rev.*, 99, 125–161,
1105 <https://doi.org/10.1016/j.earscirev.2010.02.004>, 2010.
- Simkin, S. M., Allen, E. B., Bowman, W. D., Clark, C. M., Belnap, J., Brooks, M. L., Cade, B. S., Collins, S. L., Geiser, L. H., Gilliam, F. S., Jovan, S. E., Pardo, L. H., Schulz, B. K., Stevens, C. J., Suding, K. N., Throop, H. L., and Waller, D. M.: Conditional vulnerability of plant diversity to atmospheric nitrogen deposition across the United States, *Proc. Natl. Acad. Sci. USA*, 113, 4086–4091, <https://doi.org/10.1073/pnas.1515241113>, 2016.
- 1110 Simon, H., Reff, A., Wells, B., Xing, J., and Frank, N.: Ozone Trends Across the United States over a Period of Decreasing NO_x and VOC Emissions, *Environ. Sci. Technol.*, 49, 186–195, <https://doi.org/10.1021/es504514z>, 2015.
- 1115 Simpson, D., Arneth, A., Mills, G., Solberg, S., and Uddling, J.: Ozone—the persistent menace: interactions with the N cycle and climate change, *Curr. Opin. Environ. Sustain.*, 919, 9–10, <https://doi.org/10.1016/j.cosust.2014.07.008>, 2014.
- Simpson, D. and Darras, S.: Global soil NO emissions for Atmospheric Chemical Transport Modelling: CAMS-GLOB-SOIL v2.2, *Earth Syst. Sci. Data Discuss.* [preprint], <https://doi.org/10.5194/essd-2021-221>, 2021.

1120

Soulie, A., Granier, C., Darras, S., Zilbermann, N., Doumbia, T., Guevara, M., Jalkanen, J.-P., Keita, S., Lioussé, C., Crippa, M., Guizzardi, D., Hoesly, R., and Smith, S. J.: Global anthropogenic emissions (CAM5-GLOB-ANT) for the Copernicus Atmosphere Monitoring Service simulations of air quality forecasts and reanalyses, *Earth Syst. Sci. Data*, 16, 2261–2279, <https://doi.org/10.5194/essd-16-2261-2024>, 2024.

1125

Souri, A. H., Johnson, M. S., Wolfe, G. M., Crawford, J. H., Fried, A., Wisthaler, A., Brune, W. H., Blake, D. R., Weinheimer, A. J., Verhoelst, T., Compernelle, S., Pinardi, G., Vigouroux, C., Langerock, B., Choi, S., Lamsal, L., Zhu, L., Sun, S., Cohen, R. C., Min, K.-E., Cho, C., Philip, S., Liu, X., and Chance, K.: Characterization of errors in satellite-based HCHO/NO₂ tropospheric column ratios with respect to chemistry, column-to-PBL translation, spatial representation, and retrieval uncertainties, *Atmos. Chem. Phys.*, 23, 1963–1986, <https://doi.org/10.5194/acp-23-1963-2023>, 2023.

1130

Steinbrecht, W., Kubistin, D., Plass-Dülmer, C., Davies, J., Tarasick, D. W., von der Gathen, P., Deckelmann, H., Jepsen, N., Kivi, R., Lyall, N., Palm, M., Notholt, J., Kois, B., Oelsner, P., Allaart, M., Piters, A., Gill, M., Van Malderen, R., Delcloo, A. W., Sussmann, R., Mahieu, E., Servais, C., Romanens, G., Stübi, R., Ancellet, G., Godin-Beekmann, S., Yamanouchi, S., Strong, K., Johnson, B., Cullis, P., Petropavlovskikh, I., Hannigan, J. W., Hernandez, J.-L., Rodriguez, A. D., Nakano, T., Chouza, F., Leblanc, T., Torres, C., Garcia, O., Röhling, A. N., Schneider, M., Blumenstock, T., Tully, M., Paton-Walsh, C., Jones, N., Querel, R., Strahan, S., Stauffer, R. M., Thompson, A. M., Inness, A., Engelen, R., Chang, K.-L., and Cooper, O. R.: COVID-19 Crisis Reduces Free Tropospheric Ozone Across the Northern Hemisphere, *Geophys. Res. Lett.*, 48, e2020GL091987, <https://doi.org/10.1029/2020GL091987>, 2021.

1140

Steinkamp, J. and Lawrence, M. G.: Improvement and evaluation of simulated global biogenic soil NO emissions in an AC-GCM, *Atmos. Chem. Phys.*, 11, 6063–6082, <https://doi.org/10.5194/acp-11-6063-2011>, 2011.

1145

Sun, S., Tai, A. P. K., Yung, D. H. Y., Wong, A. Y. H., Ducker, J. A., and Holmes, C. D.: Influence of plant ecophysiology on ozone dry deposition: comparing between multiplicative and photosynthesis-based dry deposition schemes and their responses to rising CO₂ level, *Biogeosciences*, 19, 1753–1776, <https://doi.org/10.5194/bg-19-1753-2022>, 2022.

1150

Tao, M., Fiore, A. M., Jin, X., Schiferl, L. D., Commane, R., Judd, L. M., Janz, S., Sullivan, J. T., Miller, P. J., Karambelas, A., Davis, S., Tzortziou, M., Valin, L., Whitehill, A., Civerolo, K., and Tian, Y.: Investigating Changes in Ozone Formation Chemistry during Summertime Pollution Events over the Northeastern United States, *Environ. Sci. Technol.*, 56, 15312–15327, <https://doi.org/10.1021/acs.est.2c02972>, 2022.

1155 Tan, J., Fu, J. S., Dentener, F., Sun, J., Emmons, L., Tilmes, S., Sudo, K., Flemming, J., Jonson, J. E., Gravel, S., Bian, H., Davila, Y., Henze, D. K., Lund, M. T., Kucsera, T., Takemura, T., and Keating, T.: Multi-model study of HTAP II on sulfur and nitrogen deposition, *Atmos. Chem. Phys.*, 18, 6847–6866, <https://doi.org/10.5194/acp-18-6847-2018>, 2018.

1160 United Nations Economic Commission for Europe: Guidance documents and other methodological materials for the implementation of the 1999 Protocol to Abate Acidification, Eutrophication and Ground-level Ozone (Gothenburg Protocol), <https://unece.org/gothenburg-protocol> (last access: 12 January 2023), 1999.

US Environmental Protection Agency (EPA): Nonattainment Areas for Criteria Pollutants (Green Book), <https://www.epa.gov/green-book>, 2023.

1165 US EPA: AQS Hourly Ozone Data, US EPA Office of Air Quality Planning and Standards/Outreach and Information Division/National Air Data Group [data set], Research Triangle Park, North Carolina, USA, available at: https://aq5.epa.gov/aqsweb/airdata/download_files.html (last access: 1 October 2024), 2024.

1170 US Global Change Research Program: Fifth National Climate Assessment, Crimmins, A. R., Avery, C. W., Easterling, D. R., Kunkel, K. E., Stewart, B. C., and Maycock, T. K. Eds., US. Global Change Research Program, Washington, DC, USA, <https://doi.org/10.7930/NCA5.2023>, 2023.

1175 van der Velde, I. R., van der Werf, G. R., Houweling, S., Eskes, H. J., Veeffkind, J. P., Borsdorff, T., and Aben, I.: Biomass burning combustion efficiency observed from space using measurements of CO and NO₂ by the TROPOspheric Monitoring Instrument (TROPOMI), *Atmos. Chem. Phys.*, 21, 597–616, <https://doi.org/10.5194/acp-21-597-2021>, 2021.

Veira, A., Kloster, S., Schutgens, N. A. J., and Kaiser, J. W.: Fire emission heights in the climate system – Part 2: Impact on transport, black carbon concentrations and radiation, *Atmos. Chem. Phys.*, 15, 7173–7193, <https://doi.org/10.5194/acp-15-7173-2015>, 2015.

1180 Vinken, G. C. M., Boersma, K. F., Maasackers, J. D., Adon, M., and Martin, R. V.: Worldwide biogenic soil NO_x emissions inferred from OMI NO₂ observations, *Atmos. Chem. Phys.*, 14, 10363–10381, <https://doi.org/10.5194/acp-14-10363-2014>, 2014.

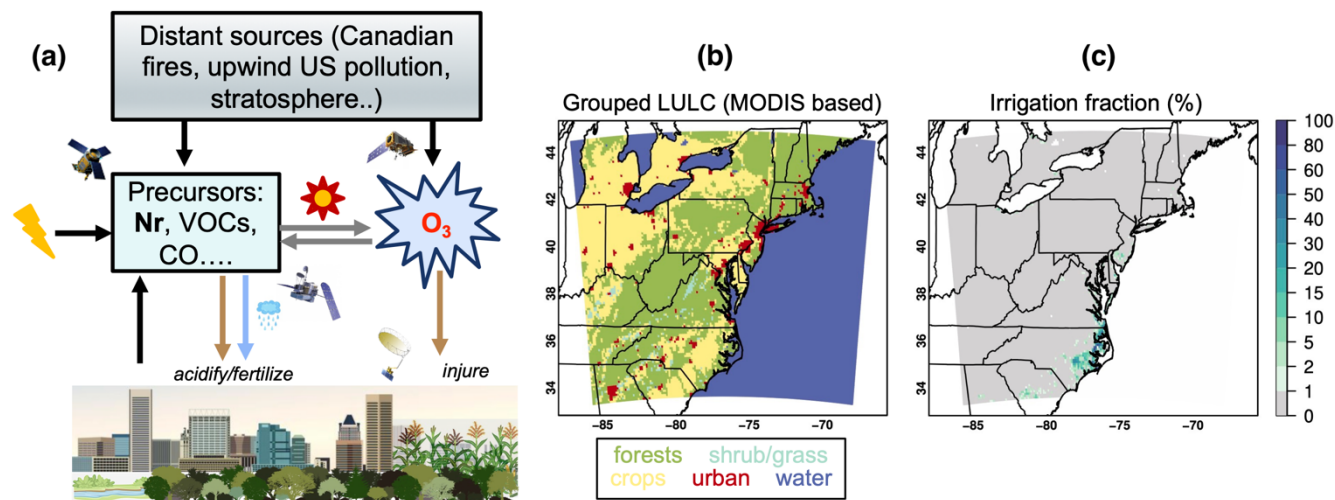
1185 Walker, J. T., Beachley, G., Amos, H. M., Baron, J. S., Bash, J., Baumgardner, R., Bell, M. D., Benedict, K. B., Chen, X., Clow, D. W., Cole, A., Coughlin, J. G., Cruz, K., Daly, R. W., Decina, S. M., Elliott, E. M., Fenn, M. E., Ganzeveld, L.,

- Gebhart, K., Isil, S. S., Kerschner, B. M., Larson, R. S., Lavery, T., Lear, G. G., Macy, T., Mast, M. A., Mishoe, K., Morris, K. H., Padgett, P. E., Pouyat, R. V., Puchalski, M., Pye, H., Rea, A. W., Rhodes, M. F., Rogers, C. M., Saylor, R., Scheffe, R., Schichtel, B. A., Schwede, D. B., Sexstone, G. A., Sive, B. C., Sosa, R., Templer, P. H., Thompson, T., Tong, D.,
1190 Wetherbee, G. A., Whitlow, T. H., Wu, Z., Yu, Z., and Zhang, L.: Toward the improvement of total nitrogen deposition
budgets in the United States, *Sci. Total Environ.*, 691, 1328–1352, <https://doi.org/10.1016/j.scitotenv.2019.07.058>, 2019.
- Wang, Y., Ge, C., Garcia, L. C., Jenerette, G. D., Oikawa, P. Y., and Wang, J.: Improved modelling of soil NO_x emissions in
a high temperature agricultural region: role of background emissions on NO₂ trend over the US, *Environ. Res. Lett.*, 16,
1195 084061, <https://doi.org/10.1088/1748-9326/ac16a3>, 2021.
- Wiedinmyer, C., Kimura, Y., McDonald-Buller, E. C., Emmons, L. K., Buchholz, R. R., Tang, W., Seto, K., Joseph, M. B.,
Barsanti, K. C., Carlton, A. G., and Yokelson, R.: The Fire Inventory from NCAR version 2.5: an updated global fire
emissions model for climate and chemistry applications, *Geosci. Model Dev.*, 16, 3873–3891, [https://doi.org/10.5194/gmd-](https://doi.org/10.5194/gmd-1200)
1200 16-3873-2023, 2023.
- Wong, J., Barth, M. C., and Noone, D.: Evaluating a lightning parameterization based on cloud-top height for mesoscale
numerical model simulations, *Geosci. Model Dev.*, 6, 429–443, <https://doi.org/10.5194/gmd-6-429-2013>, 2013.
- 1205 Wu, Z., Wang, X., Chen, F., Turnipseed, A. A., Guenther, A. B., Niyogi, D., Charusombat, U., Xia, B., Munger, J. W., and
Alapaty, K.: Evaluating the calculated dry deposition velocities of reactive nitrogen oxides and ozone from two community
models over a temperate deciduous forest, *Atmos. Environ.*, 45, 2663–2674, <https://doi.org/10.1016/j.atmosenv.2011.02.063>,
2011.
- 1210 Yao, L., Kong, S., Nemitz, E., Vieno, M., Cheng, Y., Zheng, H., Wang, Y., Chen, N., Hu, Y., Liu, D., Zhao, T., Bai, Y., and
Qi, S.: Improving below-cloud scavenging coefficients of sulfate, nitrate, and ammonium in PM_{2.5} and implications for
numerical simulation and air pollution control, *J. Geophys. Res. Atmos.*, 129, e2023JD039487,
<https://doi.org/10.1029/2023JD039487>, 2023.
- 1215 Zhang, L., Wright, L. P., and Asman, W. A. H.: Bi-directional air-surface exchange of atmospheric ammonia: A review of
measurements and a development of a big-leaf model for applications in regional-scale air-quality models, *J. Geophys. Res.*,
115, D20310, <https://doi.org/10.1029/2009JD013589>, 2010.

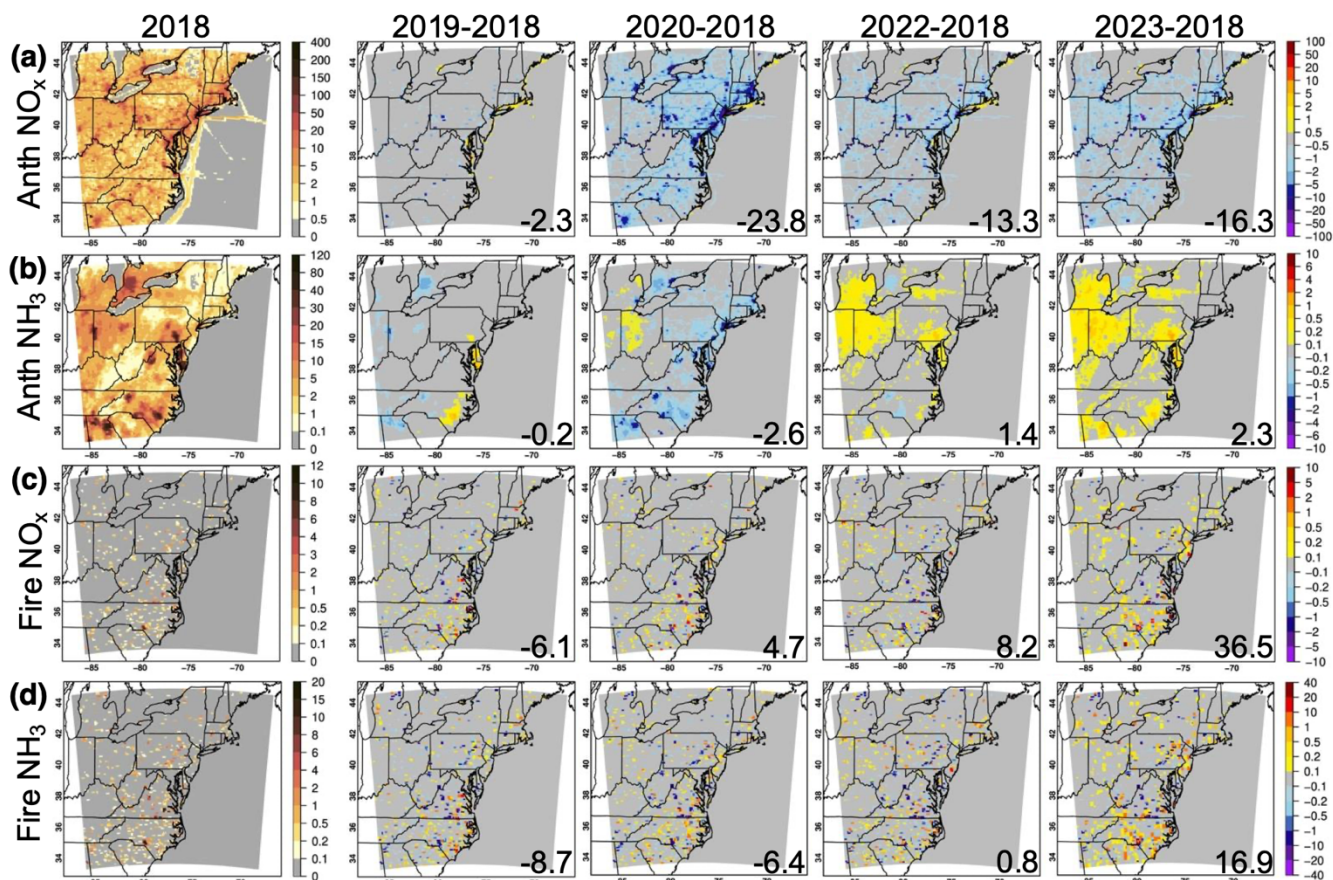
1220 Zhu, L., Henze, D., Bash, J., Jeong, G.-R., Cady-Pereira, K., Shephard, M., Luo, M., Paulot, F., and Capps, S.: Global
evaluation of ammonia bidirectional exchange and livestock diurnal variation schemes, *Atmos. Chem. Phys.*, 15, 12823–
12843, <https://doi.org/10.5194/acp-15-12823-2015>, 2015.

1225 Zhu, J. and Liang, X.-Z.: Impacts of the Bermuda High on regional climate and ozone over the United States, *J. Climate*, 26,
1018–1032, <https://doi.org/10.1175/JCLI-D-12-00168.1>, 2013.

Figures

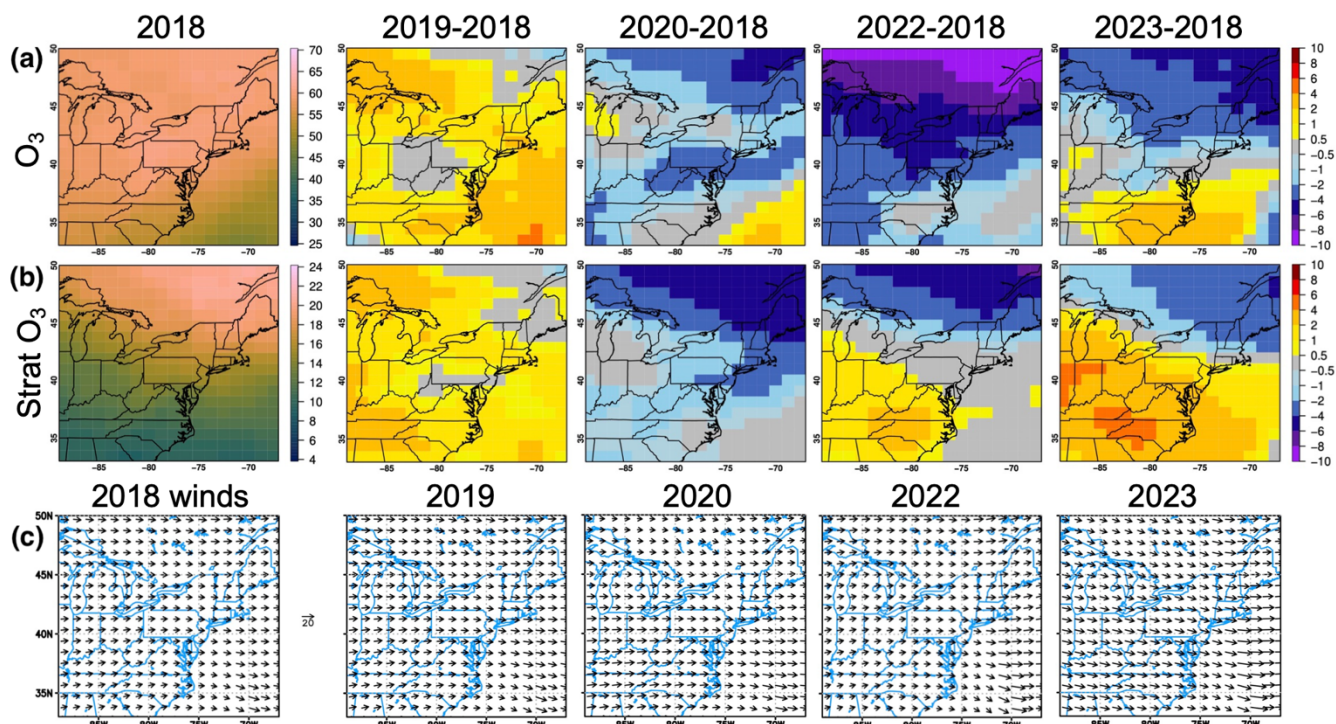


1230 **Figure 1:** (a) A simplified schematic representation of Nr-O₃ relationships in the Earth systems; (b) model domain and the grid-
dominant land use/land cover (LULC) classifications, grouped from the original 20-category International Geosphere-Biosphere
Programme-modified Moderate Resolution Imaging Spectroradiometer (MODIS) using the same criteria as in Huang et al. (2022);
and (c) irrigation fraction information required in the irrigation scheme. The grouped LULC is used for reporting potential O₃
and Nr ecosystem impacts in Section 3.2, and approximately 32%, 24%, 1%, 3%, and 40% of model grids belong to the grouped
forests, crops, shrub/grass, urban, and water category, respectively.

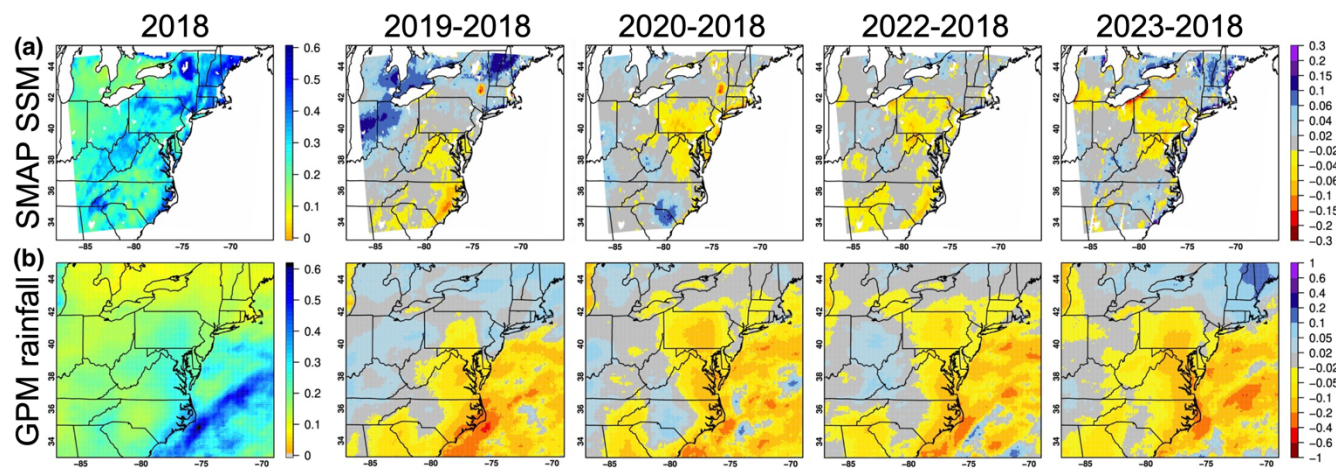


1235

Figure 2: (a;b) Anthropogenic (Anth) and (c;d) biomass burning (fire) (a;c) NO_x and (b;d) NH₃ emissions for MJJ 2018 and the differences between MJJ of each of the following years and 2018, in mol km⁻² h⁻¹. Numbers at the corners of the difference plots indicate the % changes relative to MJJ 2018.



1240 **Figure 3: MJJ ~600–800 hPa (a) total and (b) stratospheric O₃ and their interannual differences in ppbv, and (c) wind fields for each year's MJJ, from WRF-Chem's chemical boundary condition models. Stratospheric O₃ impacts on the surface are indicated in Fig. S2.**



1245 **Figure 4: (a) SMAP morning-time SSM ($\text{m}^3 \text{m}^{-3}$) on WRF-Chem grids and (b) GPM/IMERG precipitation (mm h^{-1}) on its native grid for MJJ 2018 (left) and the differences between MJJ of each of the following years and 2018. SMAP measures the globe every 2–3 days and GPM daily global-coverage products are used for this work. SMAP data are not available during 20 June–22 July 2019 due to instrument outages; and the ESA CCI version 8.1 SM product indicates qualitatively similar MJJ 2019-2018 variability.**

1250

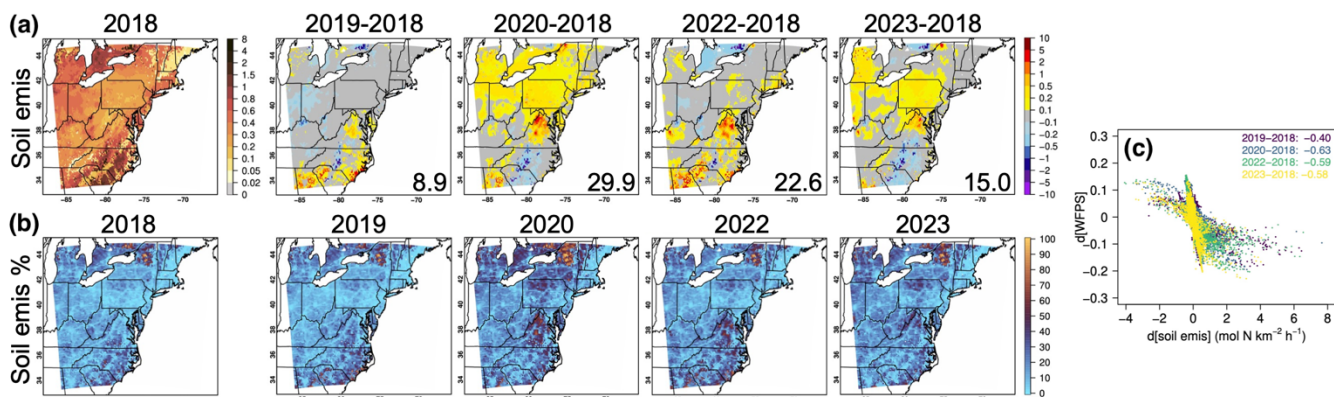


Figure 5: (a) Modeled soil NO and HONO emissions ($\text{mol N km}^{-2} \text{h}^{-1}$) and (b) soil NO and HONO emission % contributions to total anth+fire+soil NO_y emissions. Model results are averaged for MJJ 2018, shown together with the differences between MJJ of each of the following years and 2018. Numbers at the corners of the soil emission difference plots in (a) indicate the % changes relative to MJJ 2018. The scatterplot in (c) indicates relationships between the interannual differences in water-filled pore space (WFPS, whose spatial patterns are shown in Fig. S5) and soil NO_y emissions including their correlation coefficients in the upper-right legend ($p \ll 0.01$).

1255

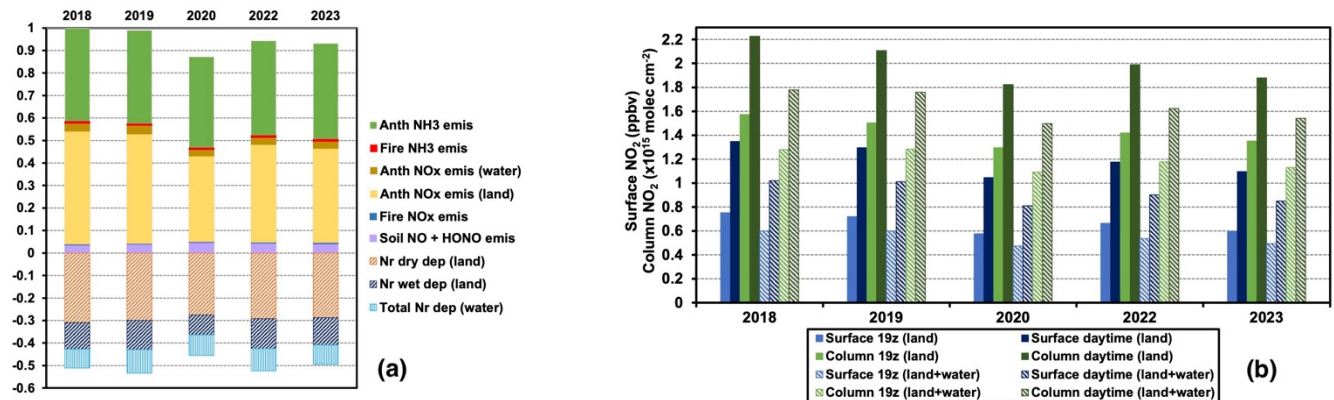
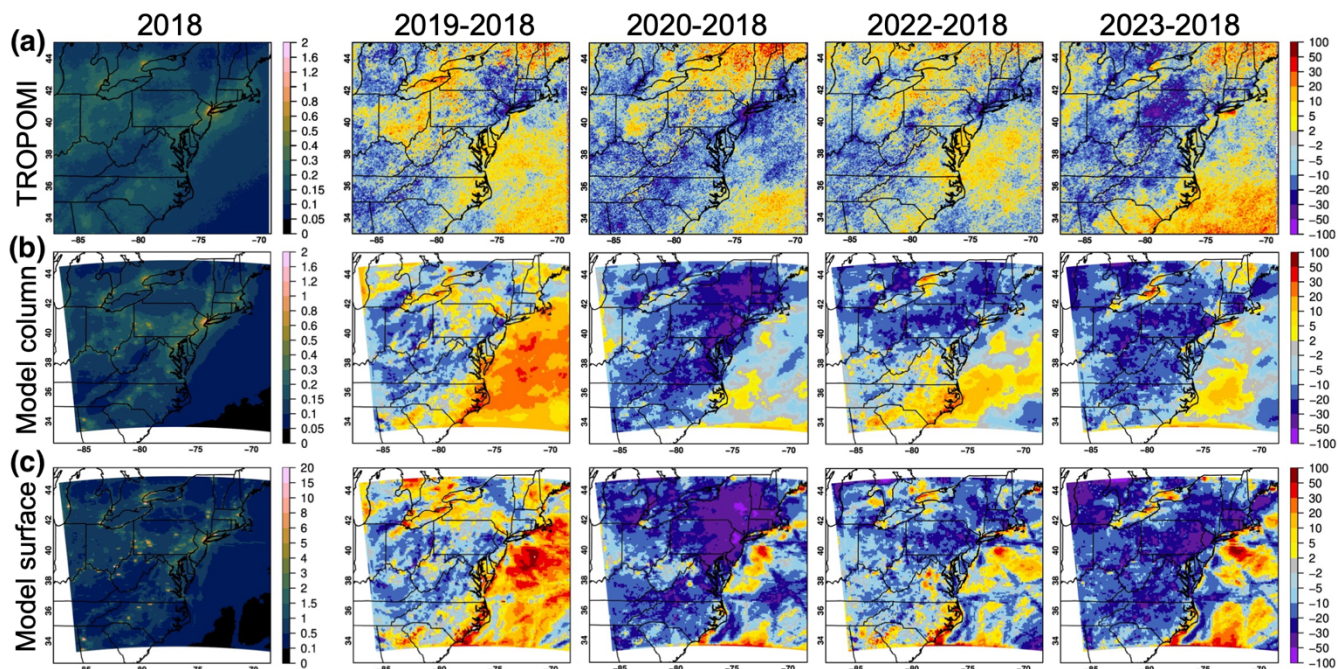


Figure 6: (a) Emission and deposition fluxes by year, scaled to MJJ 2018 total emissions; (b) Domain-wide MJJ-average surface and column NO_2 , summarized for early-afternoon (19 UTC) and daytime, and for land and all model grids. Water and land model grids are defined in Fig. 1b.

1260



1265 Figure 7: (a) TROPOMI and (b) WRF-Chem NO_2 columns; and (c) WRF-Chem surface NO_2 at 19 UTC. Results are averaged for MJJ 2018 (left, in $\times 10^{16}$ molec. cm^{-2} for column NO_2 and ppbv for surface NO_2) and shown together with the % differences between MJJ of each of the following years and 2018.

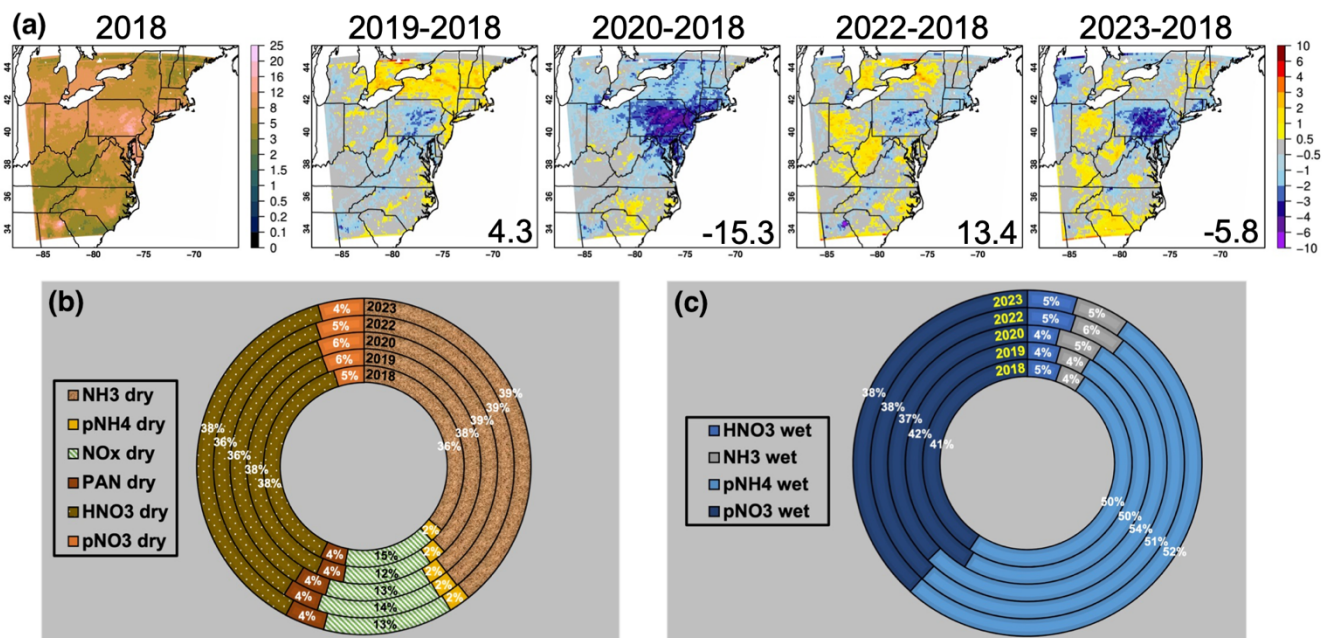
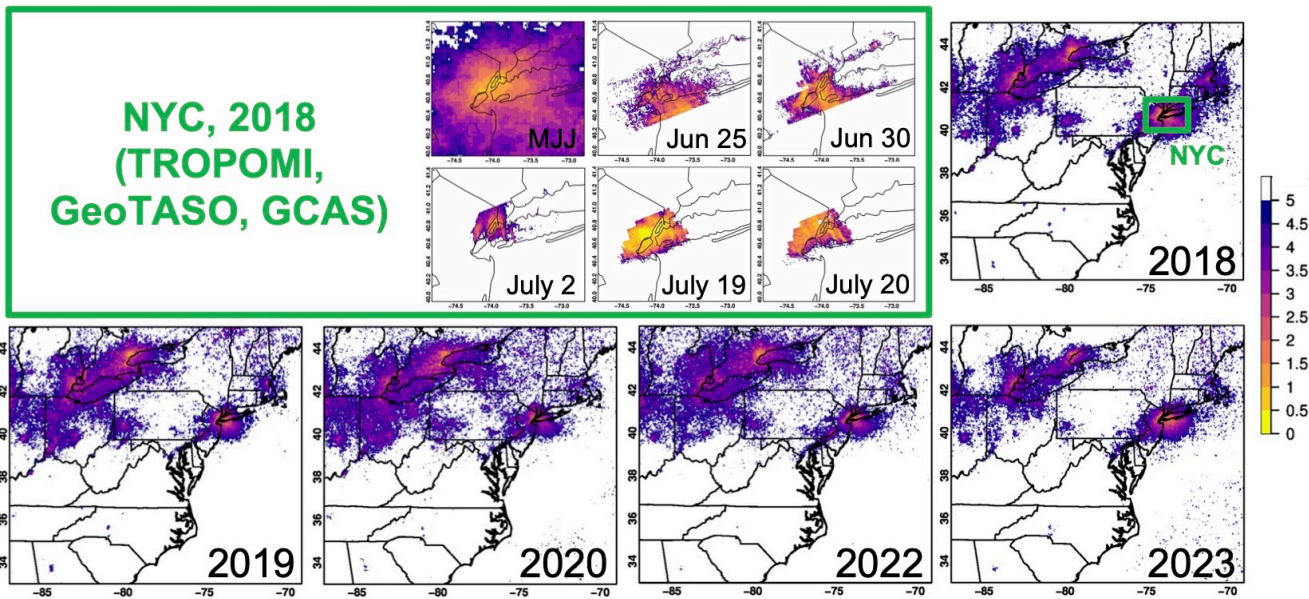
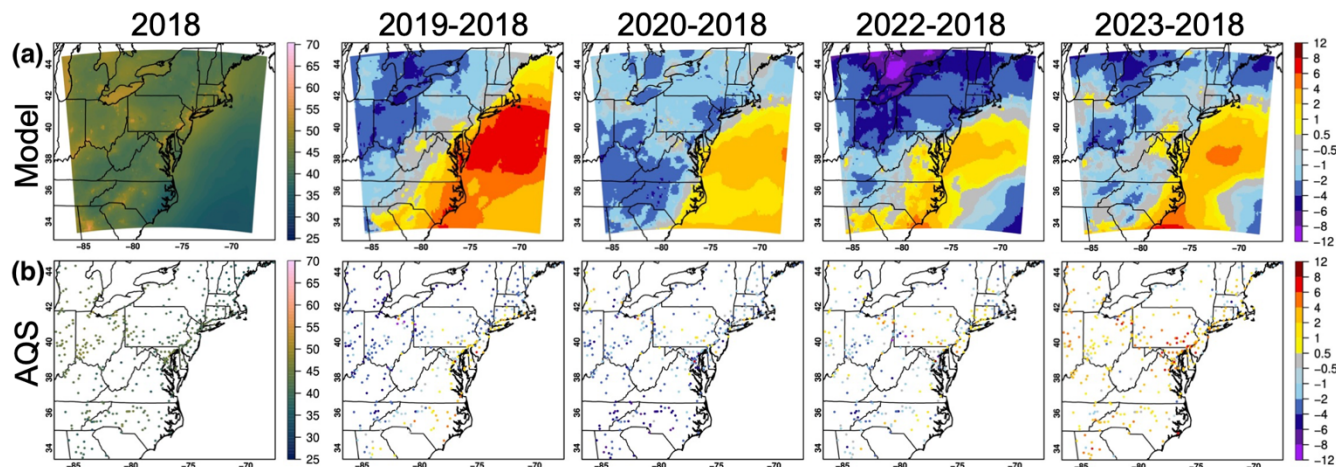


Figure 8: (a) Modeled MJJ 2018 total Nr deposition overland and differences between MJJ of each of the following years and 2018 in $\text{kgN ha}^{-1} \text{a}^{-1}$; and speciation of modeled (b) dry and (c) wet deposition fluxes by year, where prefix “p” indicates particle.



1270

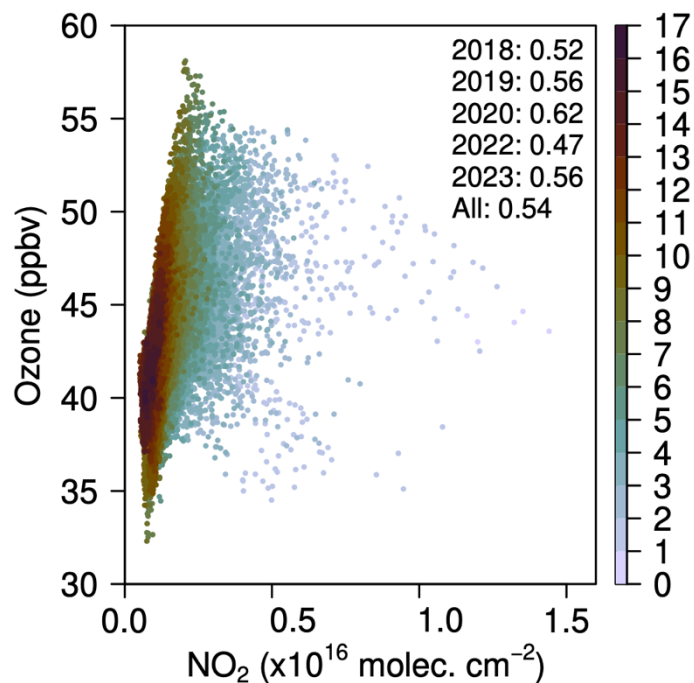
Figure 9: TROPOMI (MJJ 2018–2023), GeoTASO (25 and 30 June 2018) and GCAS (2, 19 and 20 July 2018) HCHO/NO₂ ratios. GeoTASO and GCAS both took measurements over the Greater New York City (NYC) several times during the sampling days which indicate subdaily variability in HCHO, NO₂ and their ratio. Their measurements closest to 19 UTC are used here.



1275

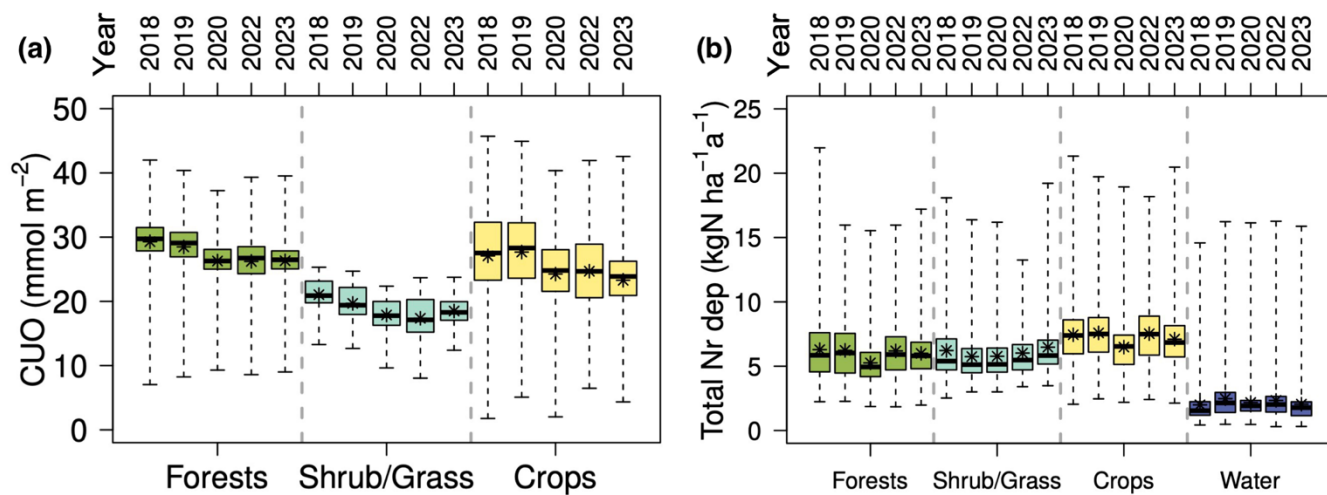
Figure 10: (a) WRF-Chem modeled and (b) AQS daytime surface O₃. Results are averaged for MJJ 2018, shown together with the differences between MJJ of each of the following years and 2018, all in ppbv. Observations from the AQS sites having <10% missing data for each year were used for evaluation. Model vs. AQS RMSEs (number of grids having collocated observations) for 2018, 2019, 2020, 2022, 2023 are 5.6 (375), 6.5 (377), 5.9 (373), 4.8 (370), and 4.0 (381), respectively.

1280



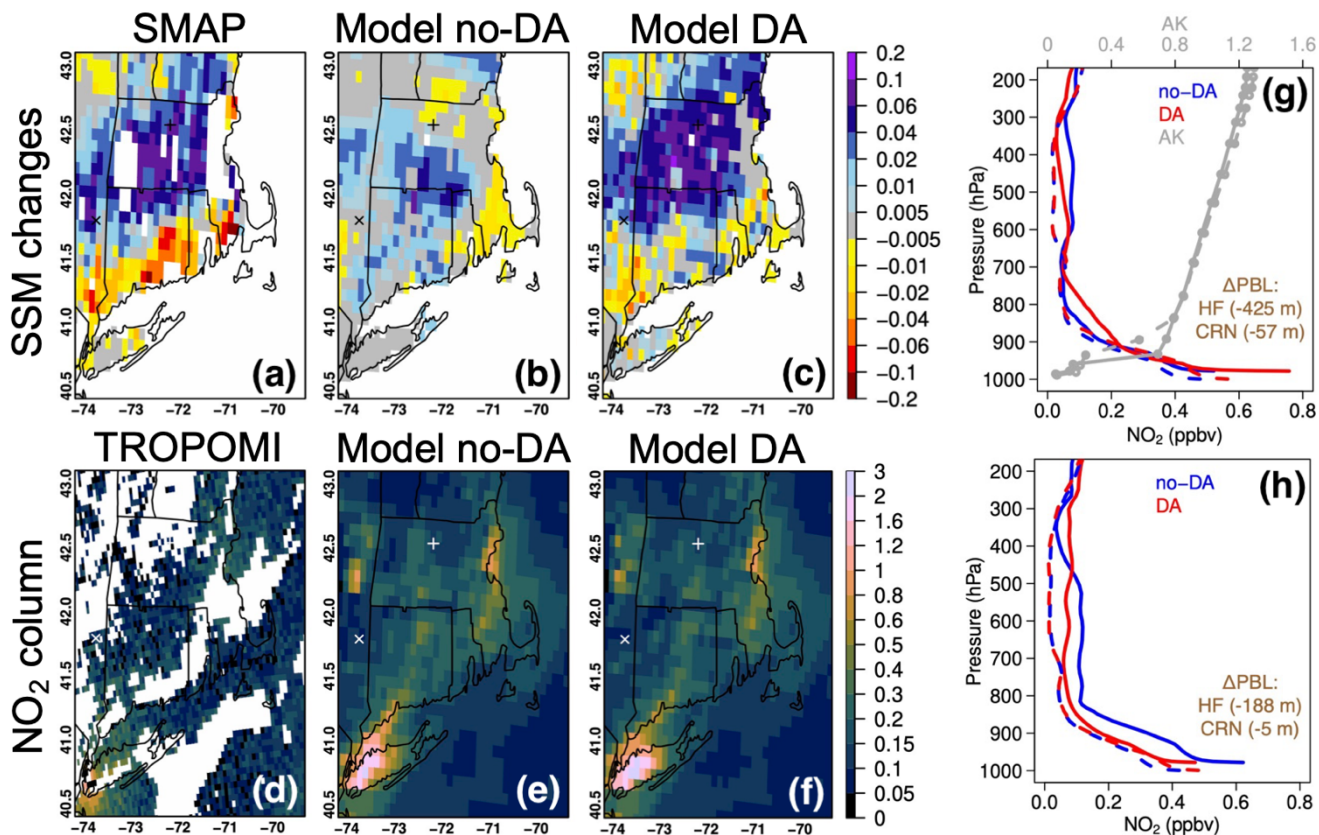
1285

Figure 11: Scatterplot indicating the relationships between WRF-Chem modeled daytime surface O₃ and 19 UTC NO₂ column during MJJ 2018–2023 for all terrestrial model grids, colored by column HCHO/NO₂ ratios. Their correlation coefficients ($p < 0.01$) are indicated in the corner legend by year.

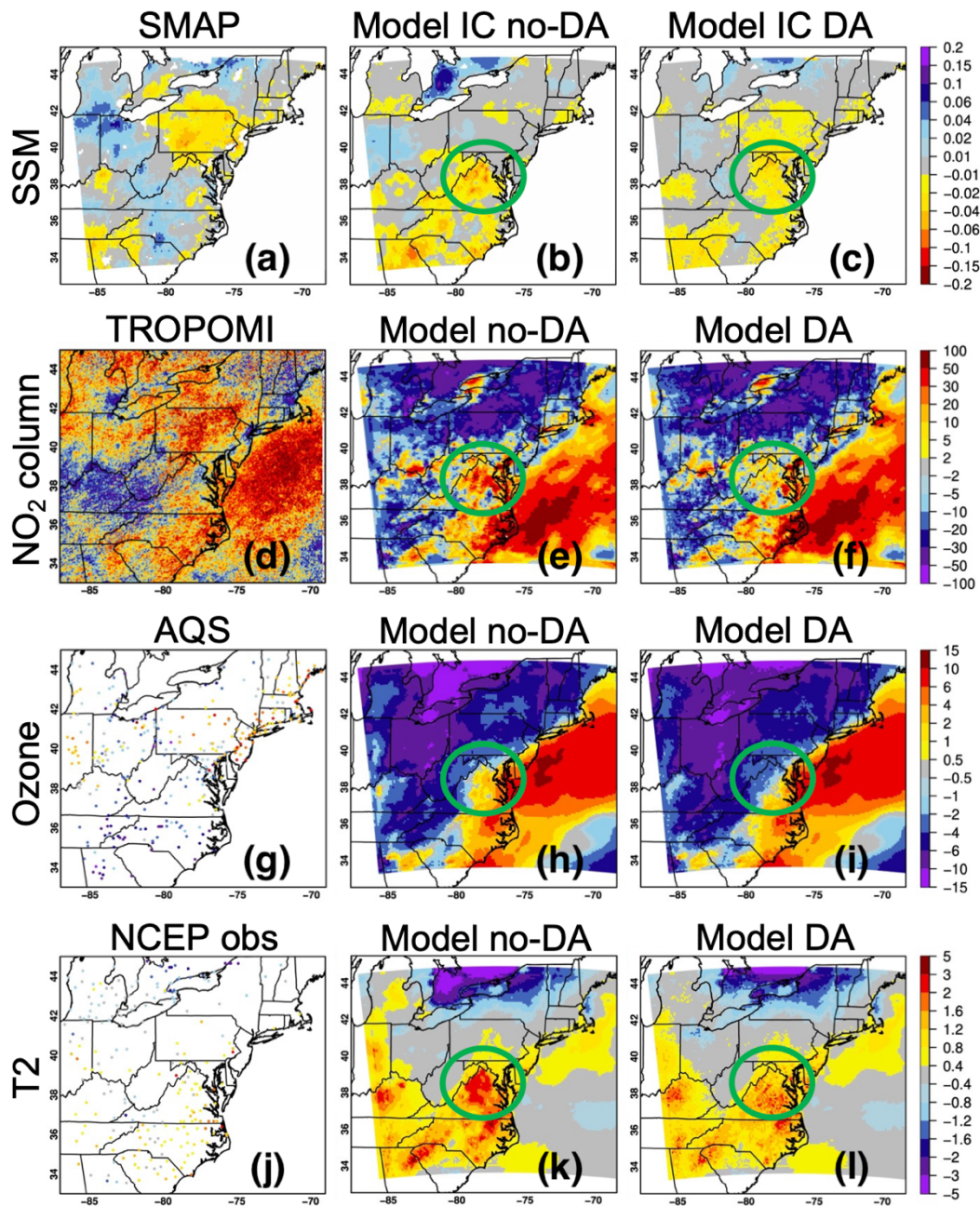


1290

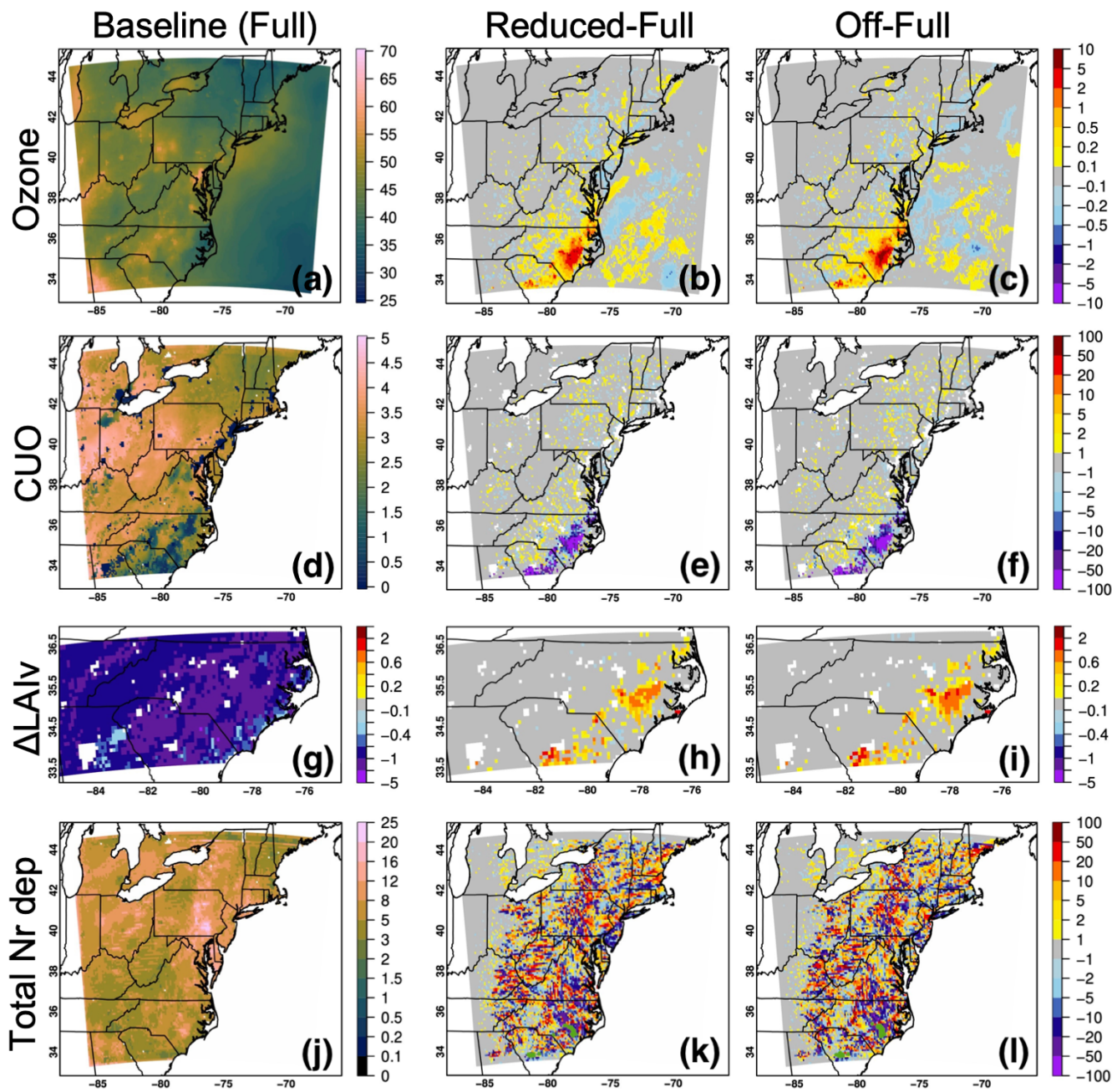
Figure 12: Box-and-Whisker plots of (a) CUO and (b) mean total Nr deposition fluxes for MJJ 2018–2023 by the grouped surface types defined in Fig. 1b.



1295 Figure 13: (a–c) 14 July–11 July SSM ($\text{m}^3 \text{m}^{-3}$) changes indicated by bias-corrected SMAP, free-running and SMAP-constrained
 Noah-MP results; (d–f) 14 July TROPOMI NO₂ columns ($\times 10^{16} \text{ molec. cm}^{-2}$) collected between 18–19 UTC, free-running and
 1300 SMAP-constrained WRF-Chem results at 18 UTC; NO₂ vertical profiles from free-running and SMAP-constrained WRF-Chem at
 Harvard Forest (HF, solid line) and CRN-Millbrook (dash line) at (g) 18 UTC and (h) 19 UTC on 14 July, along with the impact of
 SMAP DA on modeled boundary layer height (PBL) as well as TROPOMI averaging kernels (AK) on TROPOMI’s *a priori* model
 grid. The white + and × signs in (a–f) denote the locations of HF and CRN-Millbrook where in situ precipitation and SSM data are
 also analyzed. Ground-based SSM measurements on 11 July and 14 July near SMAP overpasses are 0.170 ± 0.059 and 0.245 ± 0.080
 $\text{m}^3 \text{m}^{-3}$ at HF, and 0.067 and 0.086 at CRN-Millbrook, respectively. Precipitation and ground-based O₃ fields on 11 and 14 July are
 shown in Fig. S17.



1305 Figure 14: July 2022-July 2018 monthly differences in (a–c) SSM ($\text{m}^3 \text{m}^{-3}$) indicated by bias-corrected SMAP, free-running and
 SMAP-constrained WRF-Chem initial conditions (ICs); (d–f) early afternoon NO₂ columns (%) based on TROPOMI, free-
 1310 running and SMAP-constrained WRF-Chem results; (g–i) daytime surface O₃ concentrations (ppbv) based on AQS observations,
 free-running and SMAP-constrained WRF-Chem results; and (j–l) daytime surface air temperature (K) based on the National
 Centers for Environmental Prediction (NCEP) Surface Observational Weather Data product, free-running and SMAP-
 constrained WRF-Chem results. Green circles highlight areas in/around Virginia where improvements in WRF-Chem land ICs
 notably improved the weather, NO₂ and O₃ fields. Additional information on the SMAP data assimilation (DA) impacts is included
 in Fig. S18.



1315 Figure 15: (a) Daytime surface O_3 concentration (ppbv, with the RMSE relative to AQS data of ~ 5.6 ppbv); (d) period-cumulated O_3 stomatal uptake (mmol m^{-2}); (g) O_3 impacts on leaf biomass (%) over irrigated areas in/around the Carolinas; and (h) total Nr deposition overland ($\text{kgN ha}^{-1} \text{a}^{-1}$) from the baseline simulation during 21–30 June 2022, and (b;c;e;f;h;i;k;l) their sensitivities to adjustments in irrigation schemes. Sensitivity results are in ppbv for surface O_3 concentration, and in % for all other plots. Green areas in (k;l) marked the grids where Student's t -tests comparing Nr deposition from the baseline and sensitivity simulations gave smaller-than-0.05 p values.

1320

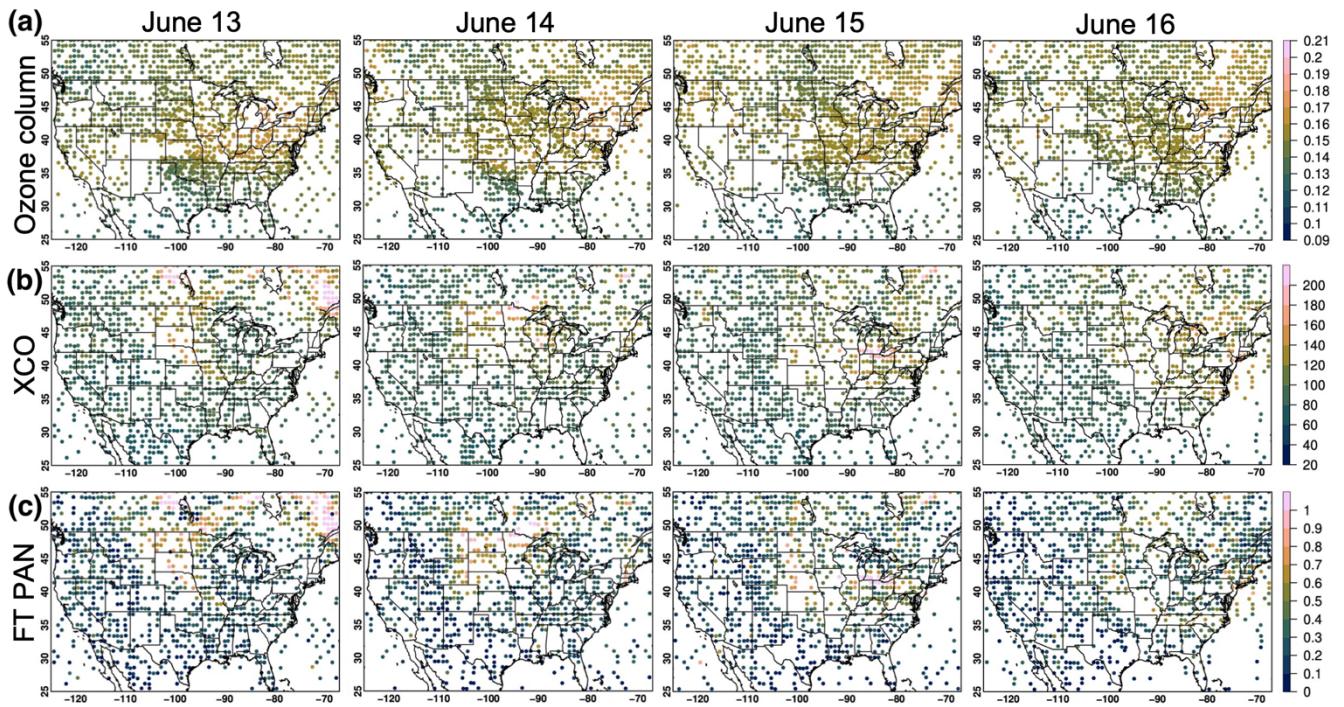
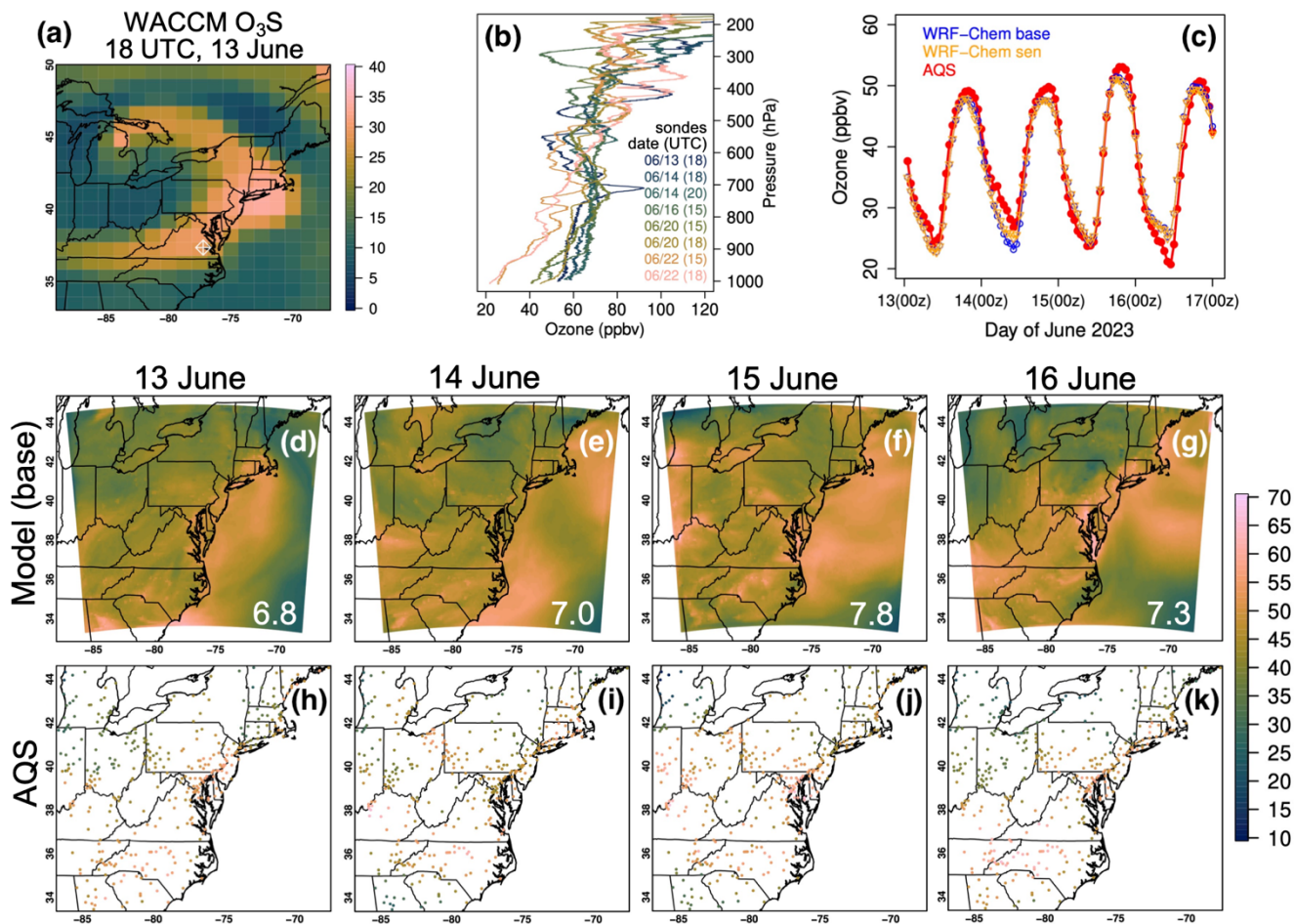


Figure 16: JPSS-1/CrIS observed (a) O₃ columns (mol m⁻²); (b) column-averaged CO mixing ratios (ppbv); and (c) column-averaged PAN mixing ratios (ppbv) for the free troposphere between 825 and 215 hPa, during 13–16 June 2023.



1325

Figure 17: (a) WACCM model stratospheric O₃ tracer (ppbv) results at ~700h Pa at 18 UTC of 13 June 2023, with location of the RRC site being indicated by a white diamond; (b) Ozonesonde profiles launched from the RRC; (c) Timeseries of the domain-mean observed and WRF-Chem modeled hourly surface O₃ during 13–16 June 2023 at AQS sites; and daytime surface O₃ concentrations (ppbv) on 13–16 June 2023 from (d–g) the WRF-Chem baseline simulation and (h–k) AQS sites. WRF-Chem vs. AQS RMSEs (ppbv) are indicated in the lower-right corners of (d–g).

1330

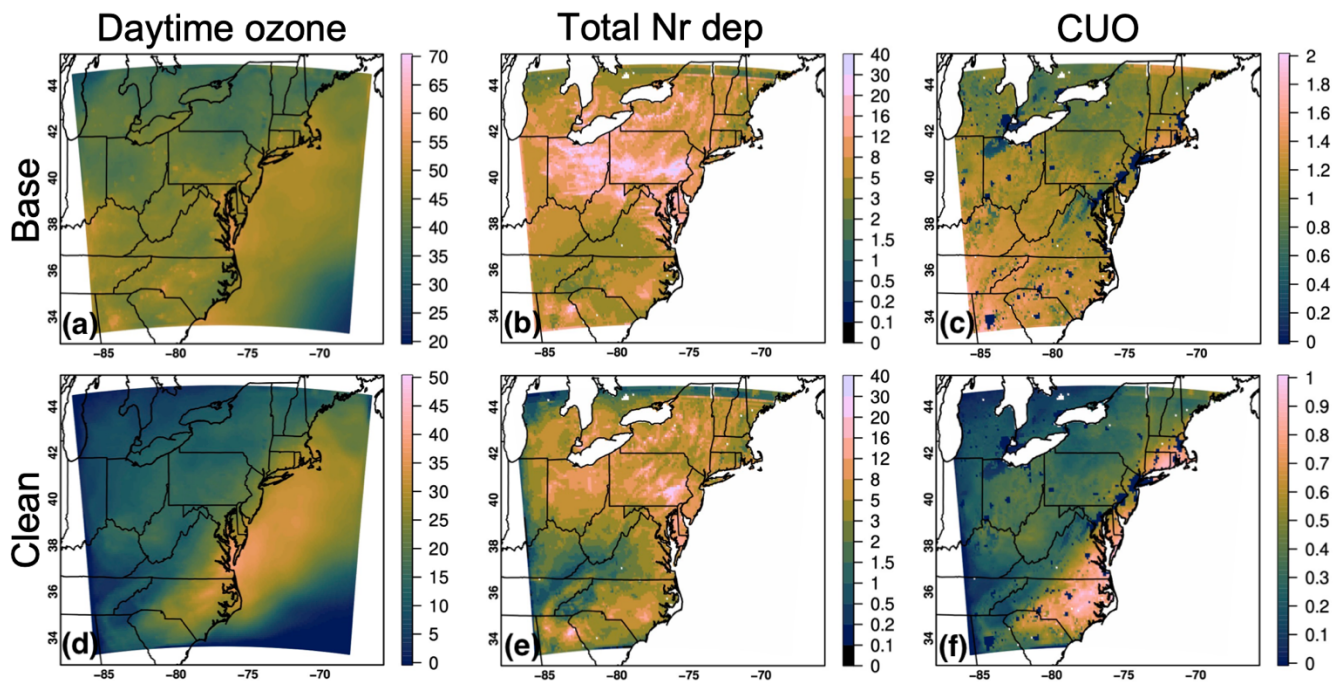


Figure 18: (a;d) Daytime surface O₃ concentrations (ppbv); (b;e) total Nr deposition overland (kgN ha⁻¹ a⁻¹); and (c;f) period-cumulated O₃ stomatal uptake (mmol m⁻²) during 13–16 June 2023 from the (a–c) baseline simulation and (d–f) sensitivity simulation with clean chemical BCs.

1335